Science
AAAS

Supplementary Materials for

Nuclear envelope rupture and repair during cancer cell migration

Celine M. Denais[1,†], Rachel M. Gilbert[1,†], Philipp Isermann[1,†], Alexandra L. McGregor[1], Mariska te Lindert[2], Bettina Weigelin[2], Patricia M. Davidson[1], Peter Friedl[2,3,4], Katarina Wolf[2], Jan Lammerding[1,*]

[1]Nancy E. and Peter C. Meinig School of Biomedical Engineering & Weill Institute for Cell and Molecular Biology; Cornell University; Ithaca, NY; USA

[2]Department of Cell Biology; Radboud University Medical Center; Nijmegen, The Netherlands

[3]Department of Genitourinary Medical Oncology, The University of Texas MD Anderson Cancer Center; Houston, TX; USA

[4] Cancer Genomic Center, The Netherlands (CGC.nl)

*Correspondence to: jan.lammerding@cornell.edu

†Authors contributed equally.

This PDF file includes:

- Materials and Methods
- Figs. S1 to S15
- Captions for Movies S1 to S7

Other Supplementary Materials for this manuscript includes the following:

- Movies S1 to S7

Materials and Methods

Cells and cell culture.

The breast adenocarcinoma cell line MDA-MB-231 (ATCC HTB-26) and the non-tumorigenic mammary epithelial cell line MCF10A were purchased from American Type Culture Collection (ATCC); the fibrosarcoma cell line HT1080 (ACC315) was purchased from the DSMZ Braunschweig, Germany; the osteosarcoma cell line U2OS was a kind gift from Marcus Smolka; the SV40-immortalized human fibroblasts were purchased from the Coriell Institute. MDA-MB-231 cells were cultured in Minimum Essential Medium Eagle (MEM, ThermoFisher Scientific) supplemented with 10% (v/v) fetal bovine serum (FBS, Seradigm VWR) and 1% (v/v) penicillin and streptomycin (PenStrep, ThermoFisher Scientific). MCF-10A cells were maintained in Dulbecco's Modified Eagle Medium (DMEM): Nutrient Mixture F-12 (DMEM/F12) supplemented with 5% horse serum (ThermoFisher Scientific), 20 ng/mL human epidermal growth factor (hEGF; Goldbio), 0.5 mg/mL hydrocortisone (Sigma Aldrich), 10 µg/mL bovine insulin (Gemini Bio Products) and 100 ng/mL cholera toxin (Sigma Aldrich). HT1080, human skin fibroblasts, and U2OS cells were grown in DMEM supplemented with 10% FBS and 1% PenStrep (complete medium) and optionally L-glutamine (1 mM) and pyruvate (2 mM). All cell lines were cultured under humidified conditions at 37°C and 5% CO_2.

Generation of fluorescently labeled cell lines.

All cell lines were stably modified with lentiviral vectors to express the nuclear rupture reporter NLS-GFP (pCDH-CMV-NLS-copGFP-EF1-blastiS) or NLS-RFP (pCDH-CMV-3xNLS-TagRFP-T-EF1-blastiS; alternatively used pmCherry2-CMV-3xNLS-mCh2 and ptdTomato-CMV-3xNLS-tdTom). Some cell lines were additionally modified to stably or transiently co-express one or more of the following constructs (vectors listed in parenthesis): NES-GFP (pCDH-CMV-NES-mNeonGreen-NES-EF1-puro); BAF-GFP (pCDH-CMV-BAF-mNeonGreen-EF1-puro); H2B-RFP (pCDNA3-CMV-H2B-mcherry, kind gift from Dennis Discher)(*33*); RFP-53BP1: pCDNA3-EF1-mCherry-53BP1-blasticidine (kind gift from Galit Lahav and Alexander Loewer)(*20*); GFP-lamin A (pCDH-CMV-BlastiS-P2A-prelamin A); GFP-lamin C; CFP-lamin A: mTurquoise-lamin A (pmTurquoise-C1 plasmid provided by Joachim Goedhart); GFP-lamin B1 (pCDH-CMV-BlastiS-P2A-lamin B1); GFP-lamin B2 (pCDH-CMV-BlastiS-P2A-lamin B2); emerin-GFP (plasmid obtained from Howard Worman); Pom121-GFP (plasmid obtained from Brian Burke and Einer Hallber); CHMP4B-GFP (pCDH-CMV-CHMP4B-mNeonGreen-EF1-puro); and VPS4B-GFP (pCDH-CMV-VPS4B-mNeonGreen-EF1-puro); VPS4B^{E235Q}-GFP, an ATP-hydrolysis mutant which still binds to ESCRT III subunits without promoting their disassembly (pCDH-CMV-VPS4B^{E235Q}-mNeonGreen-EF1-puro)(*34*); cGAS-RFP (pCDH-CMV-cGAS$^{E225A/D227A}$-mCherry2-EF1-blastiS. cGAS is a cytosolic DNA binding protein; we used a cGAS mutant (E225A/D227A) with abolished enzyme activity and interferon production, but that still binds DNA)(*16*).

For the generation of a stable clonal cell line for in vivo experimentation, GFP-lamin A (in pEGFP-C1 vector, provided by Jos Broers) was transfected by Lipofectamine 2000 and selected with neomycin for stable expression. Afterwards the cell line was cloned by limiting dilution in the presence of neomycin, and clone 1 was selected for stable, but moderate lamin expression distributed in the NE as ring-like structure with occasional intranuclear distribution (Fig. S7A-C).

Viral modification.

Pseudoviral particles were produced as described previously (*35*). In brief, 293-TN cells (System Biosciences, SBI) were co-transfected with the lentiviral plasmid and lentiviral helper plasmids (psPAX2 and pMD2.G, gifts from Didier Trono) using PureFection (SBI), following manufactures protocol. Lentivirus-containing supernatants were collected at 48 hours and 72 hours after transfection, and filtered through a 0.45 µm filter. Viruses were further concentrated using PEG-it Virus Precipitation Solution (SBI), following the manufacturer's protocol. Cells were seeded into 6-well plates so that they reached 50-60% confluency on the day of infection and transduced at most 3 consecutive days with the viral stock in the presence of 8 µg/mL polybrene (Sigma-Aldrich). The viral solution was replaced with fresh culture medium, and cells were cultured for 24 hours before selection with 10 µg/mL of puromycin or blasticidine S for 10 days. After selection, cells were subcultured and maintained in their recommended medium with 2 µg/mL puromycin or blasticidine S.

siRNA mediated depletion of lamins and ESCRT proteins.

siRNA oligonucleotide (SmartPool, containing four target sequences in one mix to reduce off-target effects) were purchased from Dharmacon (GE Healthcare): human *LMNA* (ON-TARGET plus SMART pool, L-004978-00), human *LMNB2* (ON-TARGET plus SMART pool, L-005290-00), human *CHMP2A* (ON-TARGETplus SMARTpool, L-020247-01), human *CHMP7* (ON-TARGETplus SMARTpool, L-015514-01) and non-targeting control siRNA (ON-TARGETplus non-targeting pool, D-001810-10). MDA-MB-231 and HT1080 cells were seeded into 12 well plates at optimized density the day prior to treatment and transfected with the desired siRNAs using DharmaFECT transfection reagents according to the manufacturer's instructions at a final concentration of 100 nM. Cells were used for migration experiments at 48-96 hours after transfection. Aliquots of cells were harvested at the same time to be used for confirmation of successful protein depletion by Western blot analysis and immunofluorescence imaging.

Protein immunoblot analysis.

Protein lysates were collected and analyzed as described previously (*35*). In brief, cells were either lysed in equal cell numbers in Laemmli sample buffer (Bio-Rad) containing 0.3 M of Dithiothreitol (DTT) after trypsinization or in RIPA buffer supplemented with proteinase inhibitor (Roche). Protein content was measured in the RIPA cell lysates using a standard Bradford assay. All samples were heat-denatured (5 min at 95°C) in Laemmli sample buffer and separated by SDS-PAGE (Invitrogen). Proteins were transferred onto PVDF membranes (Millipore, IPVH00010) using semi-dry transfer method (Bio-Rad). Immuno-detection was carried out with the following primary antibodies: anti-CHMP2A (Proteintech, 10477-1-AP, dilution 1:500), anti-CHMP7 (Sigma, HPA036119, dilution 1:250), anti-lamin A/C (Santa Cruz, sc-6215, dilution 1:2000; or Acris, clone 131C1, dilution 1:1000), anti-lamin B2 (Abcam, LN43, dilution 1:1000), anti-β-tubulin (Sigma, T5168, dilution 1:4000), and anti-actin (Santa Cruz, sc-

1615 HRP, dilution 1:5000). Blots were probed with HRP-conjugated antibodies (Biorad, dilution 1:1000; Jackson Immuno Research, dilution: 1:10000).

Fabrication and use of microfluidic migration devices.

The devices were prepared as described previously (*8*). The device consists of 5 µm tall migration channels bounded by two unconfined regions with a height of 250 µm. The migration channels contain constrictions with a fixed height (either 3 or 5 µm) and varying widths, ranging from 1 to 15 µm. A stable chemotactic gradient can be rapidly established between the constriction channels to promote cell migration (*8*). Molds of the devices were prepared using two-layered SU-8 photolithography. The first layer, which contains the constrictions, was made from a 5 µm tall layer of SU-8. A bypass layer and two chambers on either side of the constrictions were made from a 250 µm tall layer of SU-8 superimposed on the first layer. The 5 µm layer was created using standard photolithography techniques with SU-8 2005, and the second layer with SU-8 2075. The finished wafers were coated with trichloro(1H, 1H, 2H, 2H-perfluorooctyl)silane to facilitate demolding. Polydimethylsiloxane (PDMS) replicas of the molds were made from Sylgard 184 using the manufacturer's recipe (1:10) and baking at 65°C for 2 hours. The resulting PDMS was demolded, cut into individual devices, and holes were created for the reservoirs and cell seeding using biopsy punches. Coverslips were cleaned by soaking in 0.2 M HCl, then rinsed with water and isopropanol, and dried with compressed air. Microfluidic devices were first assembled by plasma treating the PDMS pieces and coverslips for 5 min, then immediately placing the PDMS pieces on the activated coverslips and gently pressing to form a covalent bond. The finished devices were briefly heated on a hot plate to 95°C to improve adhesion. Devices were filled with 70% ethanol, then rinsed with autoclaved deionized water and coated with extracellular matrix proteins. For all cell lines, except HT1080, devices were coated with fibronectin (Millipore) in PBS (2-20 µg/mL) for 1-2 hours at 37°C. For HT1080 cells, devices were incubated with 50 µg/mL type-I rat tail collagen (BD Biosciences) in acetic acid (0.02 N) for 2 hours at room temperature. After the incubation, devices were rinsed with PBS and medium before loading the cells. Subsequently, devices were placed inside a tissue culture incubator for a minimum of 3-24 hours to allow cell attachment before mounting the devices on a microscope for live-cell imaging. MDA-MB-231 cells were imaged in phenol-red free Leibovitz L15 supplemented with either 2% or 10% FBS, 1% PenStrep; all other cells were imaged in phenol red-free DMEM medium supplemented with 10% (v/v) fetal bovine serum (FBS, Seradigm, VWR) and 1% (v/v) penicillin and streptomycin (Invitrogen) and 25 mM HEPES. For inhibitor treatments the medium was supplemented with either 5 µM KU-55933 (Selleckchem, S1092, a kind gift of Marcus Smolka), or 100 µM (−)-Blebbistatin (Sigma, B0560). The media reservoirs of the device were covered with glass coverslips to minimize evaporation during live cell imaging.

Collagen matrix migration assays.

Experiments studying cell migration in collagen matrices were performed either using spheroid invasion assays (human skin fibroblasts) or single cells suspended in collagen matrices (HT1080 cells and human skin fibroblasts).

Spheroid invasion assay. For the spheroid invasion assay, we followed previously established procedures (*36*). In brief, cells from confluent cultures were used to generate multicellular spheroids in 96-well round-bottom plates (Costar). For each spheroid, 50,000 cells were combined with a solution of 0.25% MethoCult (Stem Cell Technologies) and complete medium, spun down in round-bottom wells at 1,000 rpm for 5 minutes, and allowed to condense for 48 hours. Individual, well-formed spheroids were then selected for embedding into collagen matrices prepared from type I rat-tail collagen (Corning) at various densities (1.5 mg/mL to 3 mg/mL). Collagen solutions were reconstituted in complete DMEM and then neutralized with 1 N NaOH. Cells or cell spheroids were added to the collagen solution prior to polymerization, which was then allowed to polymerize at 37°C for 30 minutes before adding complete medium. For some experiments, medium was supplemented with the broad MMP inhibitor GM6001 (EMD Millipore, 20 μM)(*37*). Experiments were carried out 24-48 hours after embedding the spheroid in the collagen matrix.

Single cell invasion assays.

For the analysis of nuclear fragmentation, 40,000 cells/condition were added into collagen matrices of different densities (1.5 mg/mL to 2.5 mg/mL) with or without GM6001. Cells were allowed to migrate through the collagen for 5 days, before z-stacks of the cells were taken with a laser scanning confocal microscope (Zeiss). Maximum intensity projection images of the unfixed cells were used to quantify the number of cells that had normal, ruptured, or fragment nuclei.

For the generation of cell-free or HT1080 cell-containing collagen matrices at specified collagen concentrations (1.7 to 2.5 mg/mL), acidic collagen solution (Becton Dickinson) was supplemented with 10× DMEM and NaOH to reach a neutral pH of 7.4, and then mixed with either complete DMEM alone, or HT1080 cells suspended in complete DMEM. After polymerization at 37°C in a humidified 5% CO_2 atmosphere for 10-15 min, collagen matrices were overlaid with complete DMEM. Where indicated, MMP inhibitor GM6001 (5 μM) was added to collagen and supernatant. Cell-collagen lattices were either monitored by live-cell microscopy or cultured for 15-20 hours before fixation and immunofluorescence staining.

Micropipette devices

Microfluidic 'micropipette' aspiration devices were fabricated to induce controlled nuclear deformation and NE rupture in many cells simultaneously during live cell microscopy. Similarly to the migration devices, the micropipette aspiration devices were created using a two-step process. A first 5 μm tall layer consisting of the micropipettes themselves was created using SU-8 2005 and exposed using a GCA Autostep 200 DSW i-line Wafer Stepper. This instrument allowed precise realignment of the mask and wafer (within 1 μm) for the subsequent step. After development, a layer of SU-8 2007 was spun to a thickness of 10 μm and the pocket and device features were exposed on the stepper. These devices were then baked and developed following standard photolithography procedures and coated with trichloro(1H, 1H, 2H, 2H-perfluorooctyl)silane to facilitate demolding.

PDMS molds of the devices were cast and mounted on coverslips, as described in the section above. The PDMS aspiration devices were coated with 2% BSA and 0.2% FBS in PBS for several minutes. A cell suspension was prepared in the same solution and perfused into the device at the same pressure each time (≈4 psi), using a MCFS-EZ pressure controller (Fluigent). Cell and nuclear deformation were observed using a 20×/NA 0.8 air objective. NE ruptures were detected by leakage of NLS-RFP or NLS-GFP into the cytoplasm. Dimensions of the micropipette channels were: 5 µm height and 3 µm width.

Cell compression assay

HT1080 cells were seeded on fibronectin coated glass cover slips (22 × 22 mm) and cultured for 24 h prior to compression. Compression was carried out between two parallel glass slides, with the slide facing the cells coated with silicone oil and polished to reduce cell adherence. Compression was applied manually and held for 2-3 seconds. The glass slide assembly was carefully removed without applying shear stress to the cell layer. Nuclear envelope rupture was confirmed by leakage of NLS-GFP or NLS-RFP into the cytoplasm or accumulation of cGAS-mCherry at the rupture site. Cells were allowed to recover for 5 min in media prior to fixation. Nocodazole (2 µg/mL) or vehicle (DMSO) treatment was carried out in a subset of experiments 30 min prior to compression, and cells were recovering in the same medium.

Immunofluorescence staining.

For staining cells on 2-D substrates, cells cultured on cover slips for 24 hours were fixed with 2% PFA for 30 min at 37°C, permeabilized with PBS containing 0.5% Triton X-100 for 30 minutes at room temperature, washed, and stained with anti-lamin A/C antibody (Santa Cruz, sc-6215 (N-18), dilution 1:200). Cells in collagen matrices were fixed with 2% or 4% PFA in PBS for 30 minutes at 37°C, and rinsed three times with PBS at room temperature on a rocker to remove any fixative. The samples were permeabilized with PBS containing 0.5% Triton X-100 for 30 minutes at RT, washed, blocked with 1% BSA in PBS overnight at 37°C, and incubated for 24 hours with the primary antibody (mouse anti-γH2AX, Millipore, 05-636, dilution 1:400 in PBS; anti-lamin AC, Santa Cruz, sc-6215, dilution 1:100; mouse anti-β-tubulin, Sigma, T5168, dilution 1:500). Samples were rinsed and incubated with AlexaFluor secondary antibody, AlexaFluor647-conjugated phalloidin (Invitrogen), and Hoechst 33342 or DAPI (Sigma).

To perform immunofluorescence labeling inside microfluidic devices, cells were stimulated for several days with the chemo-attractant (EGF for MDA-MB-231 cells; PDGF for human skin fibroblasts; serum for HT1080 cells), fixed with 4% PFA, and incubated for at least 2 hours at room temperature or overnight at 4°C. After several washes with PBS, the samples were permeabilized with PBS containing 0.2% Triton X-100 for 2 hours at room temperature or overnight at 4°C. After an overnight blocking step using PBS with 3-5% BSA, cells were stained with the primary antibody (mouse anti-γH2AX, Millipore, dilution 1:400) overnight at 4°C. Following several washes, the corresponding secondary antibodies were applied inside the devices (Alexa Fluor conjugated antibodies: Invitrogen, dilution: 1:500), as well as fluorescent conjugated phalloidin (Invitrogen, dilution: 1:50) overnight at 4°C. After a Hoechst 33342 (10 µg/mL) stain for 3 hours, the devices were stored and imaged in PBS containing 0.05% NaN_3.

For immunofluorescence labeling for super-resolution imaging, cells were fixed with 4% PFA for 15 min and permeabilized in 0.1% triton X-100 for 10 min. Samples were blocked with 3% BSA in PBS for 1 h and primary antibodies were diluted 1:100 (anti-CHMP4B, Proteintech, 13683-1-AP; anti-emerin, Leica Novocastra, NCL-EMERIN; anti-lamin A/C, Abcam, ab40567 (Jol-2); anti-lamin B, Santa Cruz, sc-6217; anti-β-tubulin, Sigma, T5168). After three 10 min washes cells were incubated with AlexaFluor (488, 568, 647) secondary antibodies (Invitrogen, dilution 1:100) and washed three times for 10 min each. A post-fixation was carried out to fix the antibodies location, using 4% PFA in PBS for 5 min. After two washes with PBS the coverslips were mounted (Vector, Vectashield, H-1000) and samples were imaged within 24 h.

Fluorescence and confocal microscopy.

Microfluidic migration devices were imaged on inverted Zeiss Observer Z1 microscopes equipped with temperature-controlled stages (37°C) and CCD or sCMOS cameras (Photometrics CoolSNAP EZ, Photometrics CoolSNAP KINO, Hamamatsu ORCA-flash 4.0) using 20× air, 40× water- and 63× oil-immersion objectives. The image acquisition was automated through ZEN (Zeiss) software with imaging intervals in individual sections between 2 and 10 min. Live-cell imaging of HT1080 cells transfected with fluorescently labeled H2B, NLS, and/or lamin A migrating in collagen matrices was performed on Leica SP5 and SP8 SMD confocal microscopes with 40× or 63× water objectives at 37°C and either 5% CO_2 or in sealed chambers. Z-stacks were acquired from fluorescence, reflection and transmission channels in sequential order at indicated time steps. Imaging of cell-containing fixed or cell-free unfixed hydrated collagen matrices was performed on an Olympus FV1000 confocal microscope (40×/water objective, NA 0.8) by creating Z-stacks of 1-3 μm distance and 3-D reconstruction of fluorescence images combined with reflection or transmission signal. Pore cross-section measurement was performed as described previously (*6*).

Structural illumination (SIM) and STORM imaging

Images sequences were acquired on a Zeiss Elyra PS.1 Super Resolution microscope equipped with 405, 488, 561, and 642 nm laser lines, Definite Focus focal-drift compensation, Z-piezo stage insert for fast axial focusing, pco.edge sCMOS camera for SR-SIM and an Andor Ixon Ultra 897 EMCCD camera for STORM.

For 3-D SIM Z-stacks were acquired with a 63×/NA 1.4 oil-immersion objective using five grid rotations. Images were reconstructed and a channel alignment was performed using experimental determined values using ZEN (Zeiss).

For 3-D STORM imaging, samples were labeled with AlexaFluor 647 (CHMP4B) and AlexaFluor 488 (emerin), incubated in STORM buffer (40 mM NaCl, 160 mM Tris, 10% glucose, 1% β-mercaptoethanol, 0.01 mg/mL glucose oxidase, 0.08 mg/mL catalase) and mounted on a microscope slide using wax. 40000 images were collected in HILO-mode with 3D PALM slider using a 100×/NA 1.46 Elyra oil-immersion objective. Maximum laser intensity, 20 ms exposure and a gain of 150 for the EMCCD were used to acquire the images. Images were reconstructed using ZEN (Zeiss) and channels were overlaid for illustration purposes.

Tumor implantation and intravital two-photon microscopy.

Dorsal skin-fold chambers were transplanted on 8 to 14-week-old male Balb/c nu/nu mice (Charles River), as described (*38*). Briefly, the dorsal skin-fold chamber was mounted on a skin-flap to cover the deep dermis after surgically removing the opposite side of the skin. One day post-surgery, two small tumors per chamber were implanted by injecting a cell pellet containing 10^5 HT1080 cells stably expressing histone H2B-mcherry and NLS-GFP or GFP-lamin A. For intravital microscopy at days 4-7 of tumor growth, mice were anesthetized with isoflurane (1-3% in oxygen) and the skin-fold chamber was stably mounted on the temperature-controlled stage (37°C). Blood vessels were visualized by intravenous injection of 70 kDa dextran labeled with AlexaFluor-750 (2 mg/mouse). Imaging was performed with an Olympus XLPLN25XWMP2 25× water objective (NA 1.05; 2 mm working distance) with simultaneous excitation by 2 laser lines of 910 nm and 1130 nm. Emission was detected using the following filters: GFP, ET525/80; mCherry ET620/60; SHG, ET562/40; and Al750, ET810/90m; Chroma Technology Inc.). All animal experiments were approved by the Ethical Committee on Animal Experiments and performed in the Central Animal Laboratory of the Radboud University, Nijmegen, in accordance with the Dutch Animal Experimentation Act and the European FELASA protocol (www.felasa.eu/guidelines.php).

<u>Disruption of nuclear envelope integrity by laser ablation.</u>

We used two-photon laser ablation to locally disrupt NE integrity with precise control over the location and timing, similar to previous experiments to study plasma membrane repair (*39*). MDA-MB-231 cells transiently or stably expressing fluorescent reporter constructs were seeded on fibronectin-coated glass bottom dishes. BAF-GFP and VPS4B-GFP were stably expressed together with NLS-RFP. CHMP4B-GFP was transiently transfected with NLS-RFP. The next day, the medium was changed to phenol red-free medium containing HEPES for imaging. Laser ablation was carried out on a Zeiss LSM880 microscope equipped with 488 and 561 nm excitation laser lines for fluorescent proteins and a two-photon laser (Spectra-Physics, InSight DS+) at 780 nm for ablation. Cells were imaged with a 40×/NA 1.4 oil immersion objective (3.0× zoom and 0.76 µs pixel dwell-time). Laser ablation was carried out using the FRAP module with a single scan over the selected region of interest (ROI) with 2.06 µs pixel dwell-time. Consecutive images for the GFP- and RFP-channels were collected before and after the ablation. At 780 nm with the attenuation used for the ablation (AOM at 65%), an output of 136 mW was measured at the objective:

$$\frac{W * t}{A} = \frac{136\,\frac{mJ}{s} * 2.06\ \mu s}{0.069 * 0.069\ \mu m^2} = \frac{280.16\ nJ}{0.069 * 0.069\ \mu m^2} = 58.844\,\frac{\mu J}{\mu m^2} = 58.844 * 10^6\,\frac{J}{m^2}$$

The majority of experiments were carried out with a ROI of 9×9 or 10×10 pixels, resulting in a total energy of 22.7-28.0 µJ per ablation site. Since laser ablation can result in autofluorescence signal accumulations at the site of ablation, we verified that there was no gain in signal in the GFP-channel in the first frame post-ablation. The RFP-channel showed autofluorescence accumulations, which were most likely lipofuscin-like complexes of laser induced lipid and protein fusions (*40*) and were used to confirm the laser ablation site. To evaluate whether ESCRT and BAF accumulation were specific to NE ablation, we performed experiments with a second ablation site in the cytoplasm that was distant enough from the plasma membrane to prevent ESCRT-mediated plasma membrane repair. Lipofuscin-like complexes in the RFP-channel were detectable in both ablation regions, indicating ablation of membranes and proteins. Importantly, the ESCRT and BAF recruitment to the ablation sites was specific to the NE. For all ablation experiments the escape of NLS-RFP from the nucleus was verified by quantification of the

NLS-RFP signal gain in the cytoplasm. In case of Nocodazole treatment, cells were kept in 2 μM Nocodazole or the equivalent volume of DMSO for at least 30 min prior laser ablation. Microtubule disruption was confirmed by immunofluorescence staining.

Image analysis.

Image sequences were analyzed using ZEN (Zeiss), ImageJ, or MATLAB (Mathworks) using only linear adjustments uniformly applied to the entire image region, with one exception (Fig. 1C), where images intensities were converted by taking the square root of each pixel value. Kymographs were generated using a custom-written MATLAB script. Region of interest (ROI) intensities were extracted using ImageJ or custom-written MATLAB scripts. For confocal image stacks, images were three-dimensionally reconstructed and are displayed as maximum intensity projections of selected sub-stacks containing only the cell of interest. Graphs were generated in Excel (Microsoft), and figures were assembled in Illustrator (Adobe). For better visualization, most fluorescent single color image sequences were inverted. Nuclear rupture was detected by an increase of the cytoplasmic NLS-GFP/RFP signal, or an increase in the nuclear NES-GFP signal. The sites of NE rupture were determined by observing GFP/CFP-lamin A, BAF-GFP, or cGAS-RFP accumulation in conjunction with leakage of the NLS-RFP signal from the nucleus to the cytoplasm. To analyze the localization of nuclear rupture sites, nuclear rupture was observed in cells co-expressing GFP-lamin A and NLS-RFP, migrating through the PDMS migration device. When nuclear rupture was observed within a constriction, the location of GFP-lamin accumulation was noted and totaled. For quantification of bleb localization, the ‘front' of the nucleus was defined as the leading edge of the nucleus moving through the constriction and beyond the PDMS pillars, the ‘rear’ of the nucleus included the trailing edge of the nucleus that had yet to pass the PDMS pillars, and the ‘sides’ included any portion of the nucleus touching the PDMS pillars during rupture. To quantify the frequency of chromatin protrusions and nuclear fragmentation in cells in collagen matrices, maximum intensity projections were computed from the 3-D image stacks for a total of four areas per sample. Cells within each maximum projection image were then classified as having intact nuclei, chromatin protrusions, or fragmented nuclei.

Statistical analysis.

Unless otherwise noted, all experimental results were taken from at least three independent experiments. For nuclear rupture rate comparisons, Chi-square test of independence with Yates' correction or Fisher's exact test were used. For other comparisons, we used student’s *t*-tests (comparing two groups) or one-way ANOVA (for experiments with more than two groups) with post-hoc tests. When multiple comparisons were made, we adjusted the significance level using Bonferroni corrections. Linear regression analysis was performed to test lamin A and BAF accumulation in relation to nuclear rupture intensity. Statistical significance is reported for the slope deviating from zero. Linear regression analysis for rupture rates as function of pore size in collagen matrices and the migration device was performed on the log-log transformed data set, using either results from HT1080 cells (collagen), or pooled data from HT1080 and MDA-MB-231 cells, weighted by the number of measurements at each condition (migration device). For visualization, the linear regression results were reverse-transformed into the graph. All tests were performed using GraphPad Prism. Unless otherwise noted, * denotes $p \leq 0.05$,

** denotes $p \leq 0.01$, and *** denotes $p \leq 0.001$. Unless otherwise indicated, error bars represent the standard error of the mean (s.e.m.). For rupture rate comparisons, error bars represent the standard error (s.e.) of the binomial distribution.

Supplementary Figures:

Figure S1

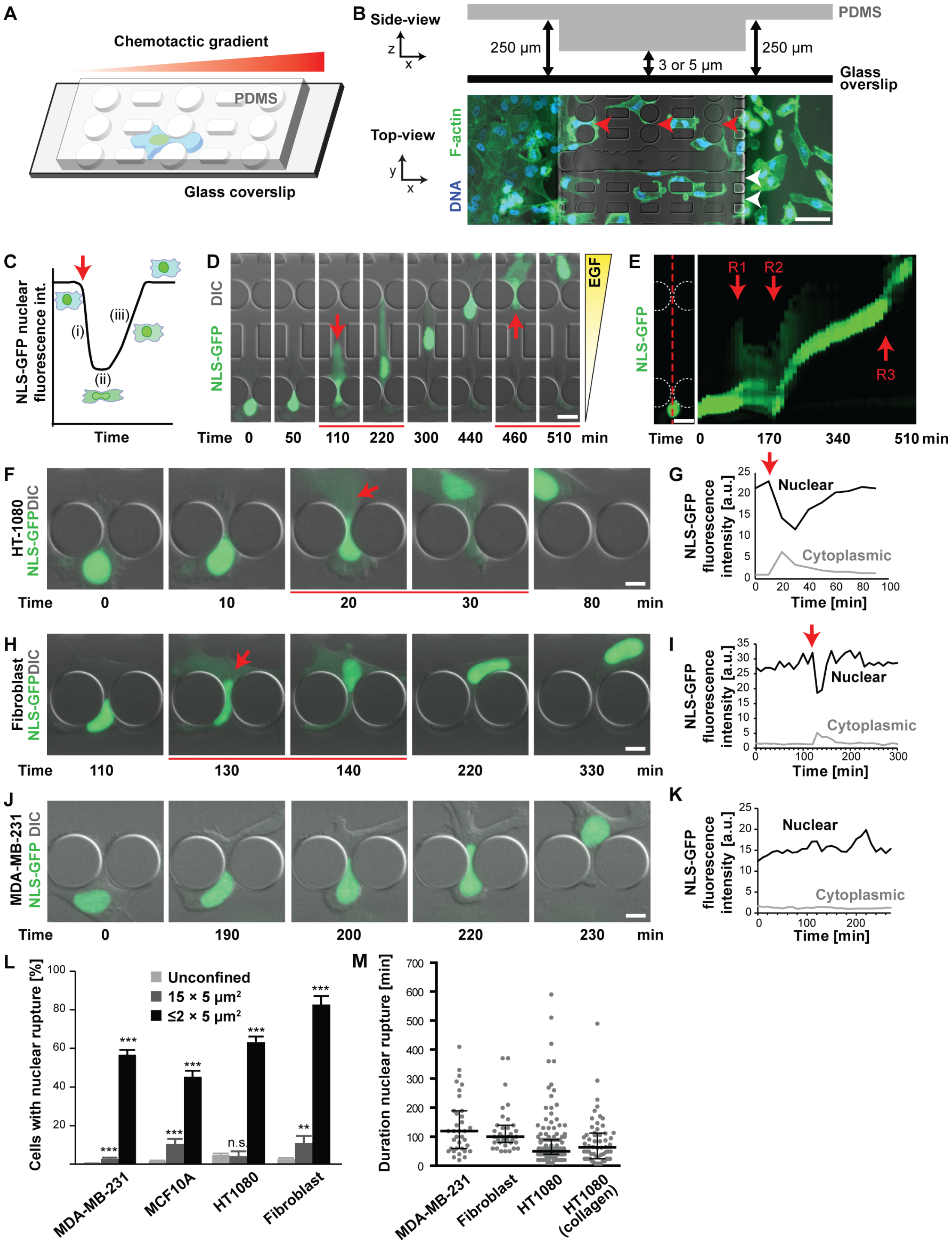

Fig. S1

Confined cell migration in microfluidic devices. (**A**) Schematic overview of the microfluidic device. Cells migrate along a chemotactic gradient through constriction channels, which provide precisely defined lateral and vertical confinement. (**B**) Top: schematic side-view marking the different heights of the unconfined regions (250 µm height) and the constriction channels (3 µm or 5 µm height). Bottom: corresponding micrograph of MDA-MB-231 breast cancer cells inside the device labeled for DNA (blue) and F-actin (green). Red arrowheads: 2 µm-wide constrictions; white arrowheads: 15 µm-wide channels. Scale bar: 50 µm. (**C**) Schematic illustration of the three phases of NE rupture and the corresponding nuclear NLS-GFP distribution: *(i)* following NE rupture (red arrow), NLS-GFP escapes from the nucleus into the cytoplasm; *(ii)* changes in nuclear NLS-GFP signal intensity level off; *(iii)* re-import of NLS-GFP into the nucleus dominates until nucleo-cytoplasmic compartmentalization is restored. (**D**) Representative image sequence of cell experiencing multiple NE ruptures while moving through sequential 5 × 2 μm^2 constrictions (reproduced from Fig. 1A). Here and in all other panels, red arrows and lines below frames indicate beginning and duration of NE rupture(s). Scale bar: 10 µm. (**E**) Corresponding kymograph along the dashed red line. R1-3 label successive rupture events. Scale bar: 20 µm. (**F, H**) Representative examples of HT1080 fibrosarcoma (F) and human skin fibroblasts (H) exhibiting migration-induced NE rupture. More than 60 cells were recorded for each cell line. Scale bar: 10 µm. (**G, I**) Corresponding NLS-GFP fluorescence signal in the nucleus (black line) und cytoplasm (gray line). (**J**) Example of an MDA-MB-231 cell migrating through a constriction without NE rupture. Scale bar: 10 µm. (**K**) Corresponding nuclear and cytoplasmic NLS-GFP fluorescence intensities. (**L**) Incidence of NE rupture for a variety of human cell lines migrating through 2 × 5 μm^2 constrictions. Measurements of cells inside the same device migrating in unconfined 2-D regions and in 15 × 5 μm^2 large channels, which require only minimal nuclear deformation, serve as comparison. **, $p < 0.01$; ***, $p < 0.001$; $n = 69–2256$ cells per condition, comparison relative to unconfined condition. Error bars: mean ± s.e. (**M**) Duration of NE ruptures, defined as the time required to restore nucleo-cytoplasmic compartmentalization of NLS-GFP, for various human cell lines studied in the migration device and in collagen matrices. Scatter plot with black lines indicating the median and interquartile range. $n = 35, 35, 140, 58$ cells, respectively.

Figure S2

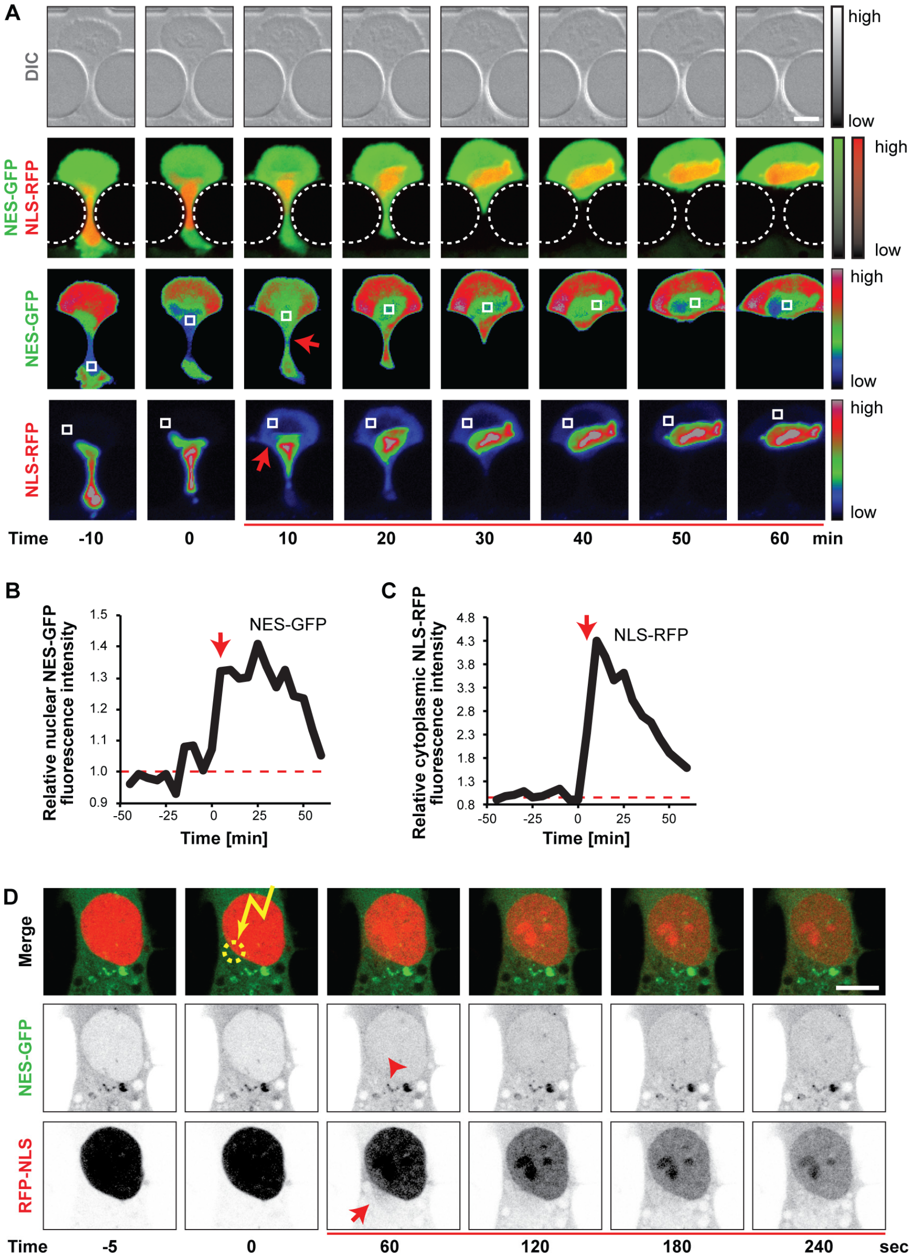

Fig. S2

NE rupture allows uncontrolled protein exchange between nucleus and cytoplasm. (**A**) Representative image sequence of an MDA-MB-231 cell (of 6 cells recorded) co-expressing NLS-RFP and NES-GFP exhibiting NE rupture during migration through narrow constriction. Here and in the other panels, red arrows and lines below frames indicate beginning and duration of NE rupture(s). NLS-RFP spilled into the cytoplasm and NES-GFP rapidly entered the nucleus. For better visualization, fluorescence intensities are displayed as a heat map, with red denoting high intensities and blue/black low intensities.

The small rectangles mark the regions of interest used for the fluorescence intensity quantification in (B) and (C). Scale bar: 10 µm. (**B, C**) Corresponding fluorescence intensity quantifications of NES-GFP (B) and NLS-RFP (C), normalized to baseline intensity (red dashed line), showing transient increase in nuclear NES-GFP and cytoplasmic NLS-RFP signals upon NE rupture. (**D**) Targeted ablation of NE segments of an MDA-MB-231 cell with a two-photon laser to confirm the specificity of the NE rupture reporters. Upon laser-induced NE rupture, NES-GFP rapidly entered the nucleus (arrowhead) and RFP-NLS escaped from the nucleus into the cytoplasm. Representative cell from 6 cells recorded. Scale bar: 10 µm.

Figure S3

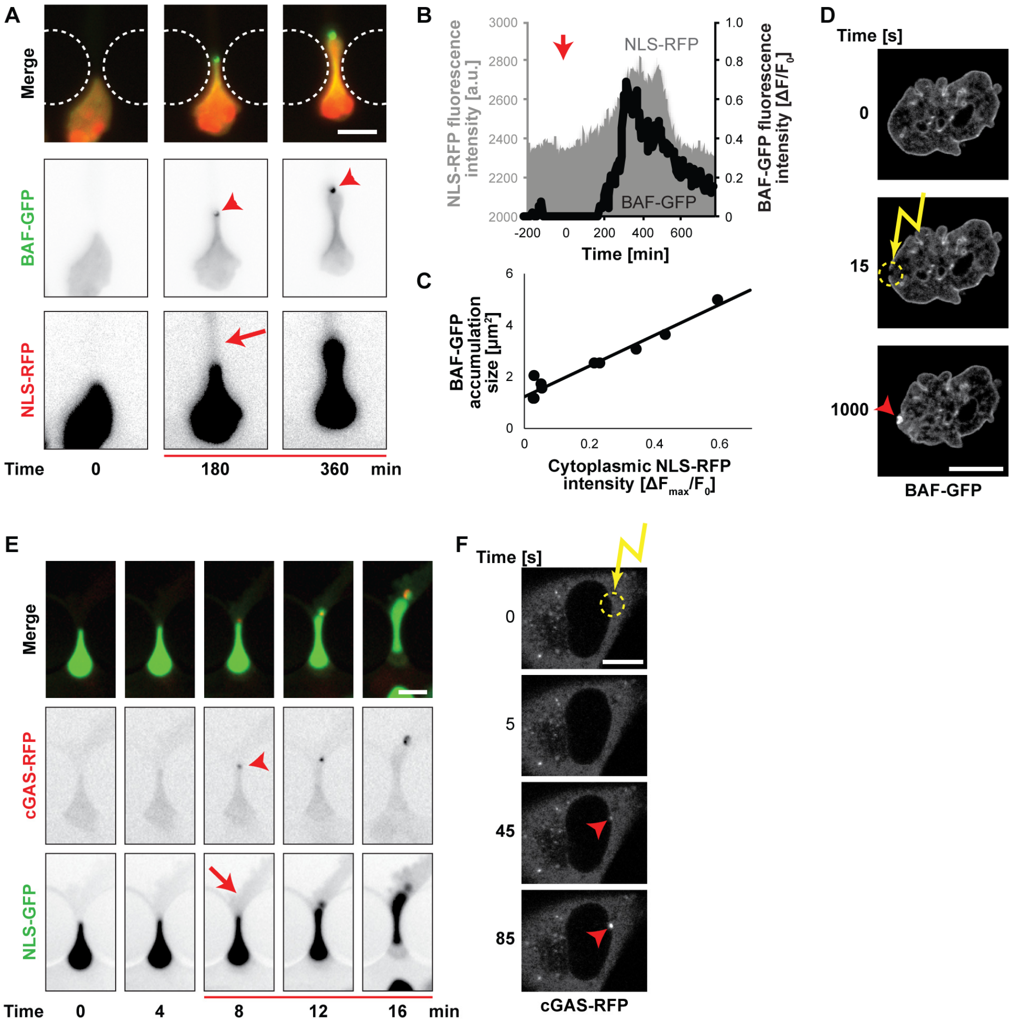

Fig. S3

Validation of BAF-GFP and cGAS-RFP as NE rupture reporters. (**A**) Representative image sequence of an MDA-MB-231 cell (out of 11 cells recorded) showing accumulation of BAF-GFP at sites of NE rupture (arrowhead). Here and in all other panels, red arrows and lines below frames indicate beginning and duration of NE rupture(s). Scale bar: 10 µm. (**B**) Corresponding quantification of the cytoplasmic NLS-RFP and BAF-GFP accumulation at sites of NE rupture. (**C**) The size of the BAF-GFP accumulation scaled linearly with the severity of the NE rupture, assessed by the extent of the NLS-RFP signal increase in the cytoplasm (slope = 5.954, $R^2 = 0.9488$, $p < 0.0001$, $n = 11$ cells). (**D**) Laser-induced NE ablation (yellow circle and flash) of an MDA-MB-231 cell expressing BAF-GFP resulted in BAF-GFP accumulation at the site of NE rupture (arrowhead). (**E**) Representative sequence (of >50 cells recorded) showing cGAS-RFP accumulation (arrowhead) at sites of NE rupture in an HT1080 cell. (**F**) Laser-induced NE rupture in an MDA-MB-231 cell caused accumulation of cGAS-RFP (arrowhead) at the site where the NE was damaged, suggesting binding of cytoplasmic cGAS-RFP to newly accessible nuclear DNA. Representative example of 4 cells recorded. Scale bar: 10 µm.

Figure S4

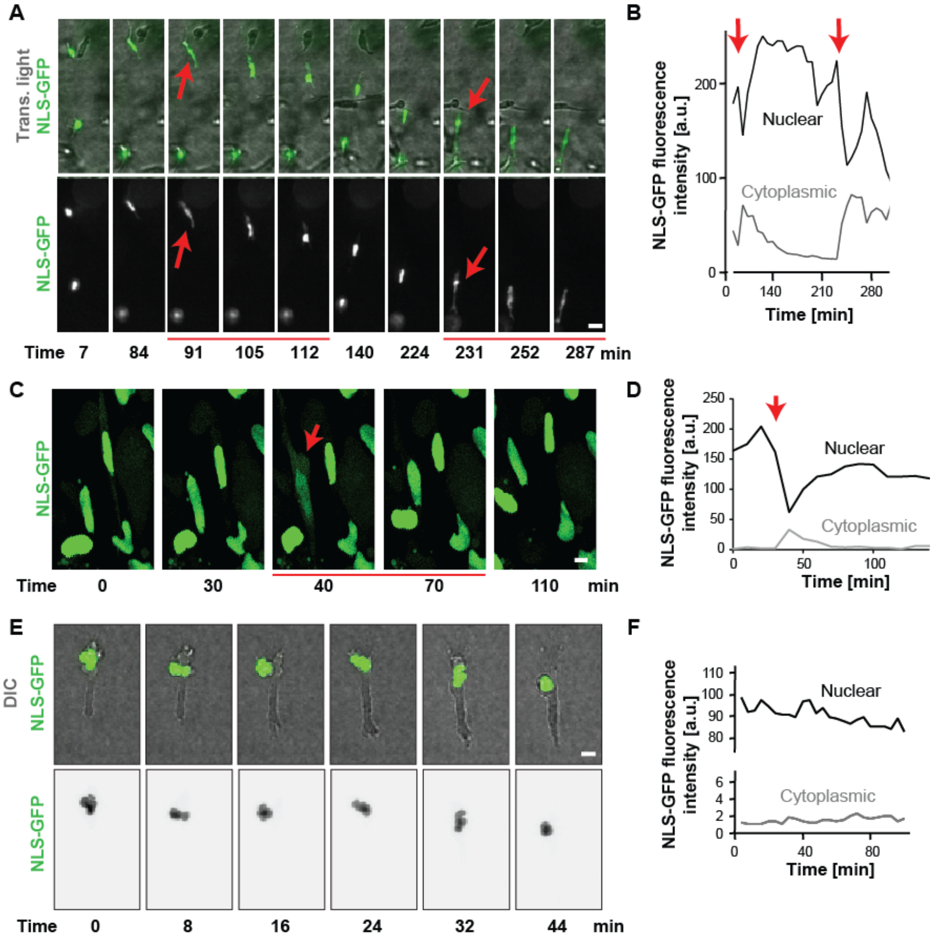

Fig. S4

Nuclear rupture during migration in collagen matrices. (**A**) Representative image sequence of HT1080 cell (out of 10 cells recorded) displaying repetitive NE rupture while migrating in collagen matrix (1.7 mg/mL + GM6001). Scale bar: 20 µm. Here and in all other panels, red arrows and lines below frames indicate beginning and duration of NE rupture(s). (**B**) Corresponding fluorescence intensity of NLS-GFP in the nucleus and cytoplasm. (**C**) Representative image sequence (maximum intensity projection) of a human skin fibroblast exhibiting NE rupture during invasion into collagen matrix (3.0 mg/mL). Four NE rupture events were recorded in total. Scale bar: 10 µm. (**D**) Corresponding nuclear and cytoplasmic NLS-GFP signal. (**E**) Representative example of an HT1080 cell migrating in collagen matrix without NE rupture (out of 3 cells recorded). Scale bar: 10 µm. (**F**) Corresponding nuclear and cytoplasmic NLS-GFP fluorescence intensity.

Figure S5

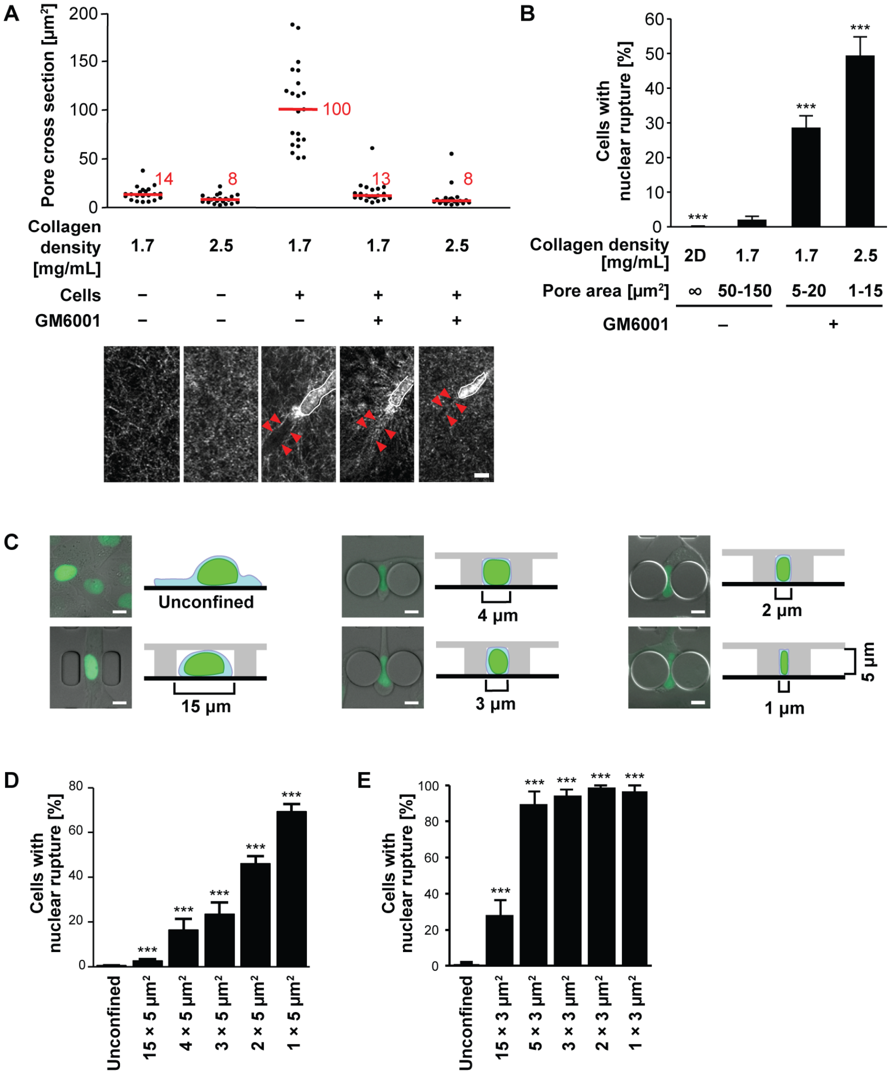

Fig. S5

Incidence of NE rupture increases with confinement. (**A**) Characterization of pore sizes in collagen matrixes as a function of collagen density and presence or absence of cell proteolytic activity. (Top) Pore size measurements at different collagen concentrations, in the absence or presence of the matrix metalloprotease (MMP) inhibitor GM6001. Red lines and numbers indicate mean value. *n* = 14-21 for each condition (Bottom) Representative examples of collagen matrix pore sizes based on reflected light imaging (from >3 independent experiments); arrowheads mark 'track' regions created by migrating cells (white lines) that locally reorganize the collagen network with MMPs, or that lack collagen reorganization in the absence of proteolytic activity. Pore sizes in cell-containing collagen matrices were measured with the area marked by arrowheads. Scale bar: 10 µm. (**B**) Incidence of NE rupture in HT1080 cells as a function of pore size in collagen matrices. ***, $p < 0.0001$ *vs.* 1.7 mg/mL collagen; 85–2992 cells per condition. (**C**) Schematic representation (side-view) and corresponding images of MDA-MB-231 cells (top-view) passing through increasingly narrower constrictions in the microfluidic migration device.

In the 5-µm tall channels the nucleus fills the height of the channel, and passage through the lateral confinement induces the largest nuclear deformation. Scale bar: 10 µm. (**D**) Incidence of NE rupture as a function of constriction size in the 5 µm tall migration channels. ***, $p < 0.0001$ *vs*. unconfined cells; $n = 55–445$ cells. (**E**) Incidence of NE rupture as a function of constriction size in the 3-µm tall migration channels. ***, $p < 0.0001$ *vs*. unconfined cells; $n = 31–459$ cells. Error bars in figure: mean ± s.e.

Figure S6

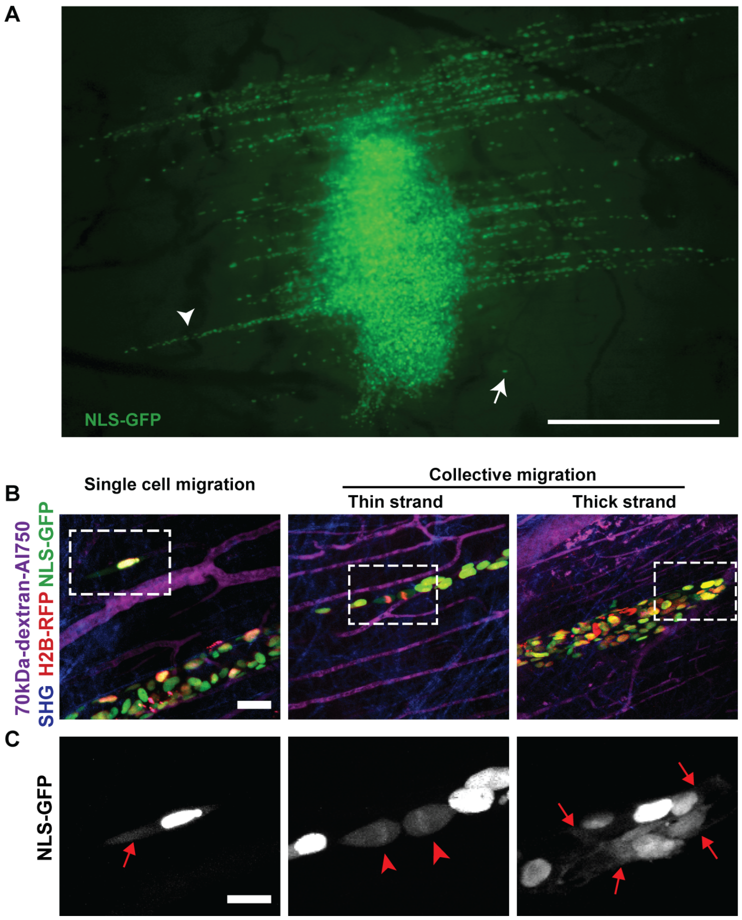

Fig. S6

NE rupture during cancer cell invasion in vivo. (**A**) Epifluorescence overview image of HT1080 fibrosarcoma infiltrating into mouse dermis 5 days after implantation. White arrow: single migrating cell; white arrowhead: invasion strand with collective migration. Scale bar: 500 µm. (**B**) Examples of invasion modes ranging from single migrating cells to compact collective invasion strands. Maximum intensity projection images showing collagen fibers detected by second harmonic generation (blue), blood vessels visualized by AlexaFluor-750 labeled 70 kDa-dextran (magenta), NLS-GFP (green), and chromatin labeled with H2B-RFP (red). Dashed lines indicate location of close-ups shown in (C). Scale bar: 50 µm. (**C**) Close-up (NLS-GFP channel) of cells exhibiting NE rupture during single cell migration (left), migration as thick collective strand (right). (Center) Mitotic cell in thin collective strand showing cytoplasmic dispersal of NLS-GFP. Scale bar: 25 µm. Red arrows indicate cells with NE rupture; red arrowheads highlight release of NLS-GFP into the cytoplasm due to NE breakdown during cell division, serving as positive control.

Figure S7

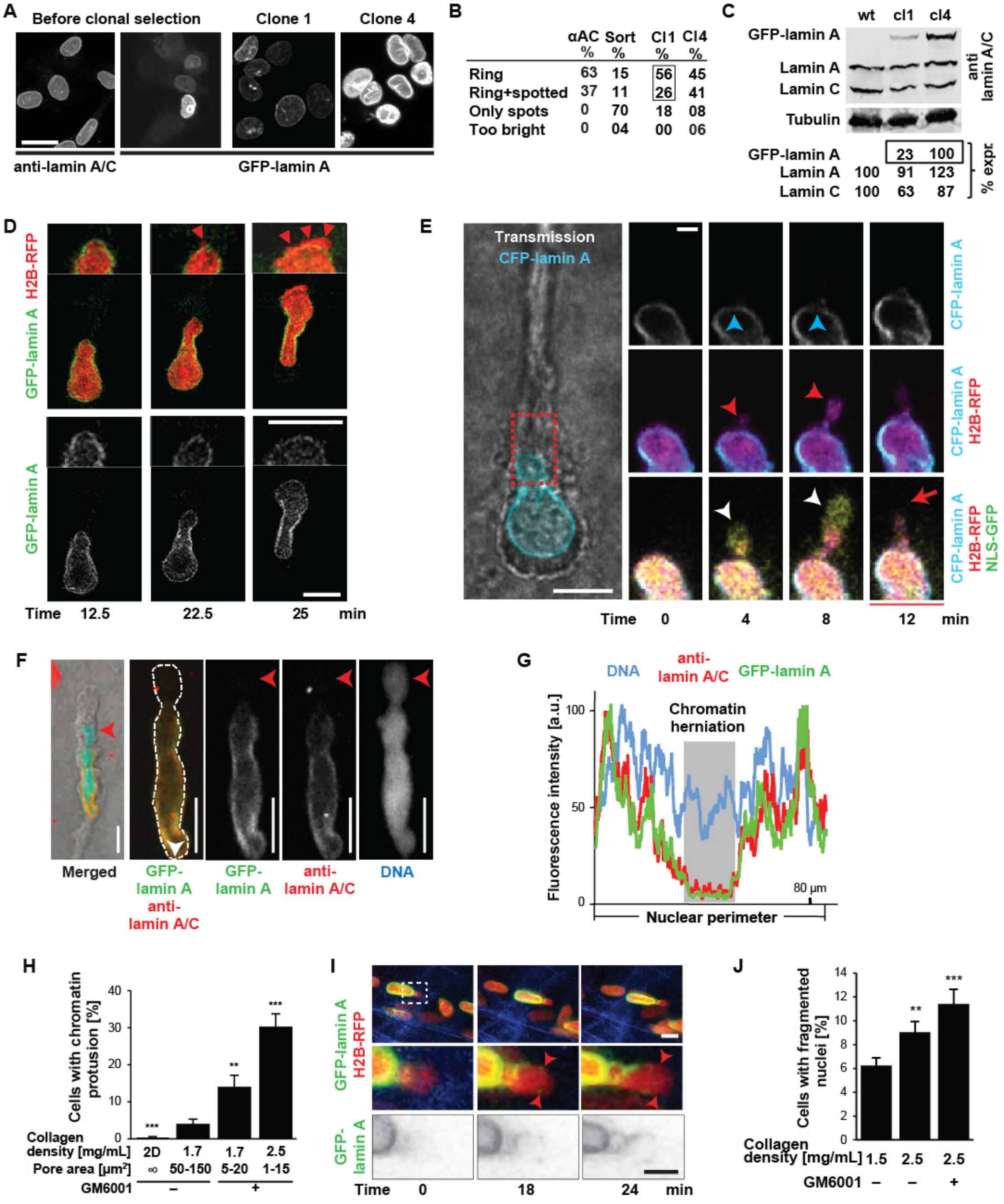

	αAC %	Sort %	Cl1 %	Cl4 %
Ring	63	15	56	45
Ring+spotted	37	11	26	41
Only spots	0	70	18	08
Too bright	0	04	00	06

% expr	wt	cl1	cl4
GFP-lamin A		23	100
Lamin A	100	91	123
Lamin C	100	63	87

Fig. S7

Chromatin protrusion and fragmentation during confined migration in collagen matrices. (**A**) Representative images of HT1080 cells stably transfected with GFP-lamin A and sorted twice (left two images). The resulting expression, however, was heterogeneous, even after repeated sorting (second image). Two clones derived from single cells showed more uniform expression (right two images). Scale bar: 20 µm. (**B**) Quantification of the lamin A localization in parental, sorted and clonal cells with (**C**) corresponding Western blot analysis for lamin A/C, with tubulin as loading control. Clone 1 cells were chosen for *in vivo* experimentation because of their moderate and uniform GFP-lamin A expression. (**D**) Image sequence and close-ups of HT1080 clone 1 cell co-expressing histone H2B-RFP and GFP-lamin A displaying chromatin protrusions (arrowheads) across the nuclear lamina during migration in collagen matrix (3.3 mg/mL + GM6001). Close-ups of selected areas form the nuclear leading edge showing chromatin herniations, and (as more evident in the corresponding Movie S4) local lamin A loss at indicated regions. Scale bar: 10 µm. (**E**) Representative image of an HT1080 cell (of 3 cells recorded) co-expressing CFP-lamin A, histone H2B-RFP, and NLS-GFP migrating into collagen matrix and showing bleb formation (white arrowhead) accompanied by a chromatin protrusion (red arrowhead) through the lamina (blue arrowhead) that partially fills the bleb. After NE rupture (red arrow, at 12 min), the nuclear blebs collapses to the level of the chromatin protrusion. Insets indicated by red box. Scale bars: 10 µm (overview) and 2 µm (inset). (**F**) Representative image of a chromatin (blue) protrusion (of 30 cells recorded) through the lamin A network (green) in an HT1080 cell expressing GFP-lamin A (clone 1) in collagen matrix. Red arrowhead indicates site of chromatin protrusion. Antibody staining for lamin A/C confirmed correct localization of GFP-lamin A; DNA stained with DAPI. Scale bar: 10 µm. (**G**) Line intensity profile along dotted line in panel (E) showing co-localization of GFP-lamin A with the immuno-stained lamin A/C. White arrowhead indicates start of line profile, with measurements continued in clock-wise direction. (**H**) Percentage of HT1080 clone 1 cells with chromatin protrusions as function of collagen matrix pore size, with unconfined (2D) migration as reference. Chromatin protrusions were detected based on H2B-RFP and GFP-lamin A localization. **, $p < 0.0033$; ***, $p < 0.003$ compared to 1.7 mg/mL collagen without MMP inhibitor (GM6001); $n = 35\text{-}2341$ cells per condition. Results closely matched those obtained with DAPI labeling and immunofluorescence staining for endogenous lamin A/C, depicted in Fig. 2C. (**I**) Example of chromatin protrusion (arrowhead) in vivo. Image depicts invading fibrosarcoma cells (clone 1) co-expressing GFP-lamin A (green) and H2B-RFP (red) migrating through collagen (blue) and recorded by intravital imaging. See also Movie S5. Inset indicated by white dashed box. Scale bars: 10 µm. (**J**) Percentage of human skin fibroblasts with fragmented nuclei during migration in collagen matrices with decreasing pore sizes. **, $p < 0.01$; ***, $p < 0.001$; $n = 692–1441$ cells per condition.

Figure S8

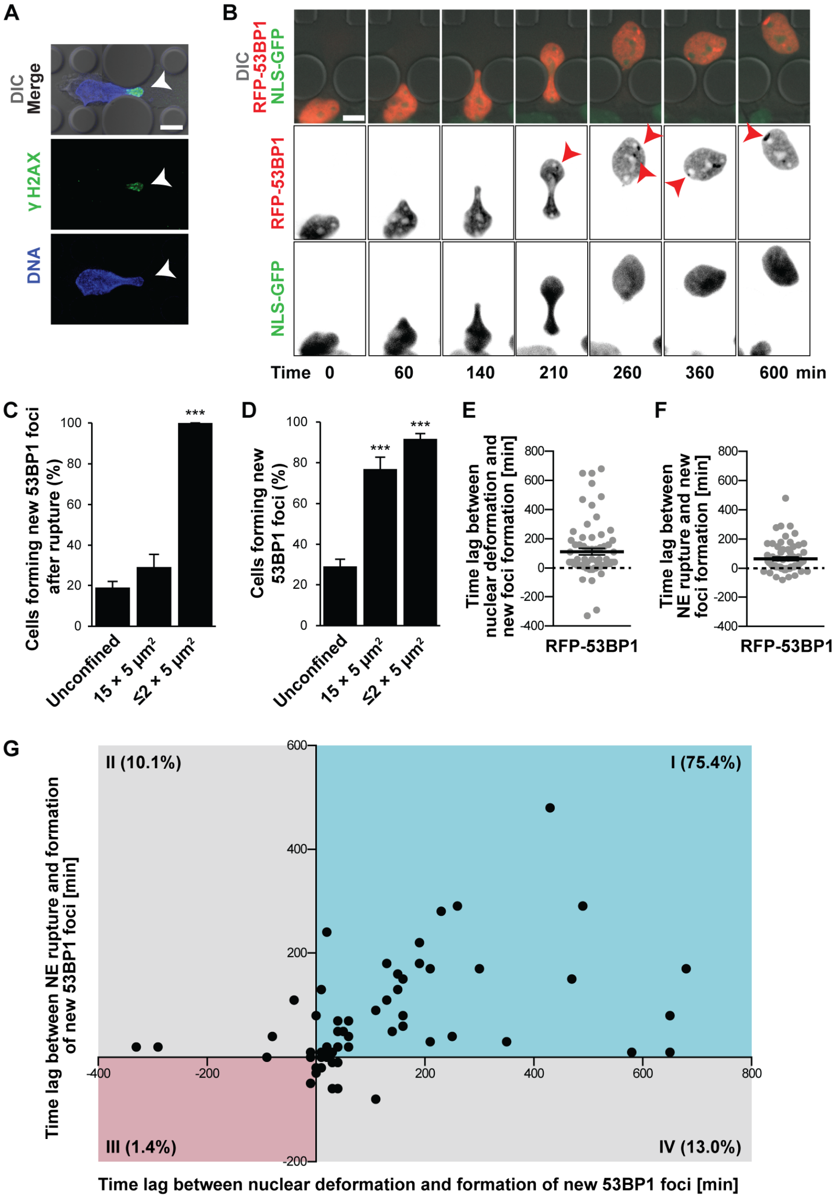

Fig. S8

Confined migration causes DNA damage. (**A**) Example of γ-H2AX-positive chromatin protrusion in the leading edge of the nucleus in an MDA-MB-231 cell migrating through a narrow constriction, indicating extensive DNA damage (arrowhead). Scale bar: 10 μm. (**B**) Representative image sequence of U2OS cell co-expressing NLS-GFP and RFP-53BP1. Migration through 2 × 5 μm^2 constrictions resulted in formation of RFP-53BP1 foci (arrowheads), indicating confined migration-induced DNA double strand breaks, even in the absence of NE rupture. All recorded cells (35 total) formed RFP-53BP1 foci when migrating through constrictions ≤ 2 μm wide and 5 μm tall. Scale bar: 10 μm. (**C**) Percentage of HT1080 cells forming RFP-53BP1 foci after NE rupture. In confined conditions, which are associated with large nuclear deformation, NE rupture resulted in more frequent formation of RFP-53BP1 foci than in less-confined or non-confined condition, suggesting that deformation of chromatin during migration through tight spaces renders DNA more susceptible to damage. ***, $p < 0.001$; $n = 21, 41, 54$ cells, respectively. (**D**) Percentage of HT1080 cells forming new RFP-53BP1 foci over a ≈12 hour observation period as a function of cell confinement, both in the absence and presence of NE rupture. Even mild confinement in 15 × 5 μm^2 channels increased the fraction of cells with newly formed RFP-53BP1 foci compared to cells in unconfined, 2-D conditions, despite the relatively low rate of NE rupture under these conditions (1.8% of cells ruptured in unconfined conditions; 15.0% ruptured in the 15-µm wide channels, and 49.5% in the ≤2-µm wide constrictions). ***, $p < 0.001$; $n = 181, 52, 109$ cells, respectively. **(E-F)** Analysis of timing between the start of nuclear deformation (E) and NE rupture (F) and the formation of new RFP-53BP1 foci in HT1080 cells migrating through ≤2-µm wide constrictions. Each dot represents a newly formed RFP-53BP1 accumulation ($n = 69$ newly formed foci observed in 29 cells total, recorded in five independent experiments). Positive values indicate that nuclear deformation/NE rupture preceded the formation of 53BP1 foci. Solid black lines mark the median and interquartile range. (**G**) Diagram plotting the results from (E, x-axis) and (F, y-axis) against each other, with each dot representing a single RFP-53BP1 accumulation event. Quadrant I represent events where both NE rupture and nuclear deformation could contributed to 53BP1 formation; quadrant II represents events in which only NE rupture could have contributed to foci formation (since nuclear deformation began after the event); quadrant III represents events where both NE rupture and nuclear deformation occurred after 53BP1 foci formation and could thus not contribute to the event; quadrant IV represents events where only nuclear deformation could contribute to 53BP1 foci formation, as NE rupture follows the event. Percentages list the distribution among the four quadrants based on the total events (69 newly formed foci observed in 29 cells total).

Figure S9

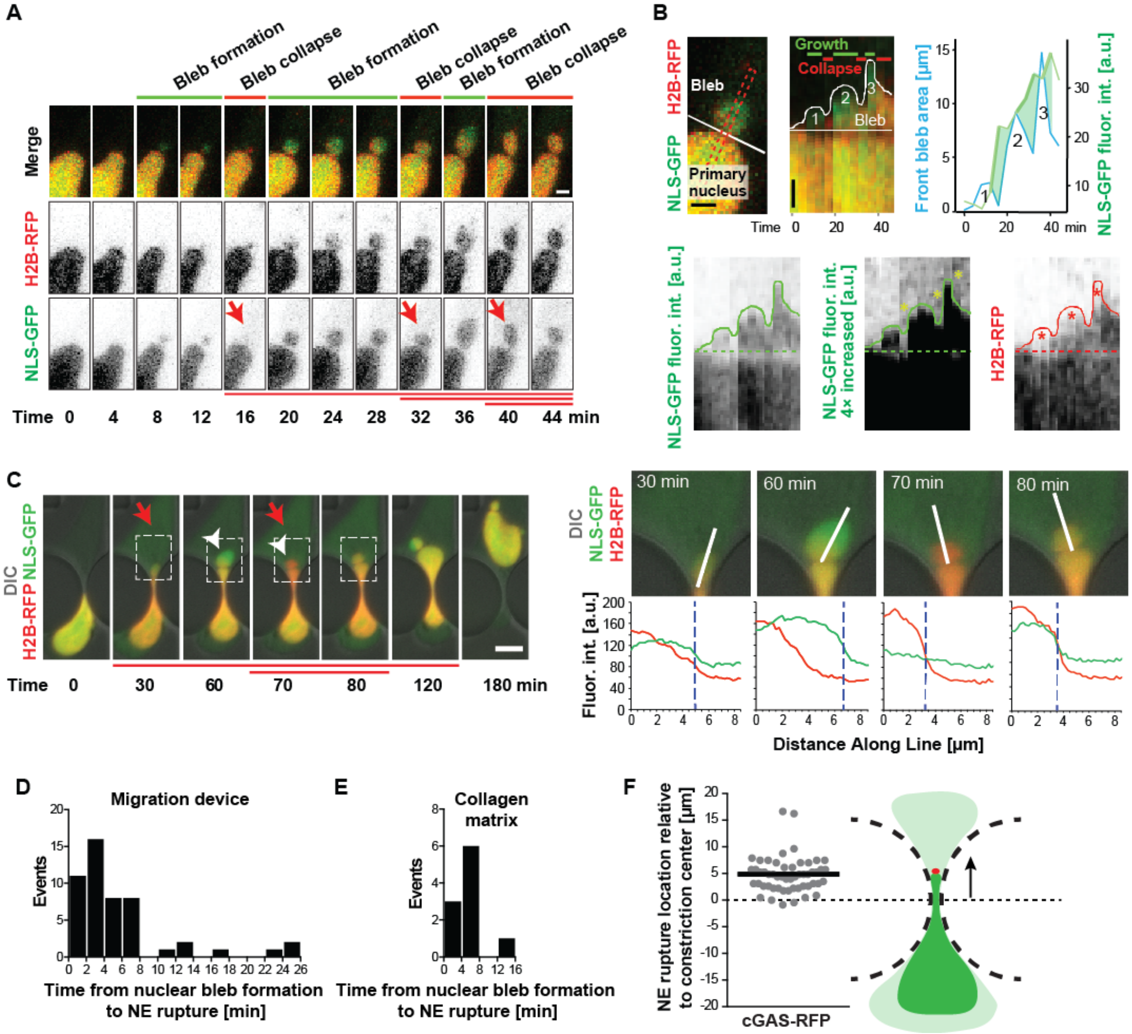

Fig. S9

NE rupture is preceded by nuclear membrane bleb formation. (**A**) Close-up of nuclear membrane bleb formation, chromatin protrusion, and bleb collapse upon rupture in an HT1080 cell co-expressing H2B-RFP (red) and NLS-GFP (green) migrating through collagen matrix (2.5 mg/mL) in the presence of MMP inhibitor GM6001. This is the same cell as shown in Fig. 1C and Movie S2. Bleb formation (green lines) precedes NE rupture. Here and in all other panels, red arrows and lines below frames indicate beginning and duration of NE rupture(s). Upon repeated NE rupture, the bleb collapses and retracts to the level at which chromatin has filled the bleb. Scale bar: 2 µm. (**B**) Detailed analysis of the membrane and chromatin dynamics during the nuclear bleb formation and collapse shown in (A). Top left: depiction of the position where the line image was taken for kymograph. Top middle: kymograph using linear images normalized in position to the base of the bleb (indicated by white line). Repeated bleb growth is designated by numbers 1-3. Top right: quantitative analysis of growing and shrinking nuclear bleb area (in blue color; measured from the bleb base on), together with cytoplasmic NLS-GFP signal intensity (green plot). Note that increases in cytoplasmic NLS-GFP intensity always coincided with nuclear bleb area shrinkage (depicted by the green filled areas), indicating release of intranuclear pressure upon NE rupture. Bottom row: respective single channels as indicated. In the NLS-GFP kymograph with 4× enhanced signal intensity (bottom center), NLS-GFP spilling into the cytoplasm is indicated by green stars. In the H2B-RFP channel (bottom right), the red stars indicate chromatin-low regions inside the bleb that are filled with NLS-GFP, as apparent from the NLS-kymograph. Scale bars: 2 µm. (**C**) MDA-MB-231 cell migrating through $1 \times 5\ \mu m^2$ constriction. Arrowheads indicate formation of nuclear membrane blebs, partially filled with chromatin (white arrow head). Upon a second NE rupture (double red line), the bleb retracts until its size coincides with the protruded chromatin (second white arrowhead). Dashed white lines indicate inset locations for images on the right, revealing nuclear membrane bleb formation and collapse. Line profile plots along the white lines of each bleb are plotted below showing the nuclear membrane (green) extends past the chromatin bleb (red) and upon rupture, the NE collapses onto the chromatin. The blue dashed line in the plot shows the furthest point of each bleb. Scale bar: 10 µm. (**D**) Histogram of the duration between nuclear membrane bleb formation and NE rupture during migration of HT1080 cells in microfluidic device. Positive values indicate that NE rupture followed nuclear bleb formation. No negative values were recorded for >40 cells analyzed. (**E**) Corresponding histogram for HT1080 cells migrating in collagen matrix, showing a similar lag of 2-8 minutes between nuclear bleb formation and subsequent NE rupture. (**F**) Analysis of NE rupture location during HT1080 cell migration through microfluidic constrictions. Scatter plot of rupture location expressed relative to the constriction center in the direction of cell migration (black arrow). Black line indicates median. The scatter plot only contains NE rupture events at the front of the nucleus, which represented >95% of all events in these cells.

Figure S10

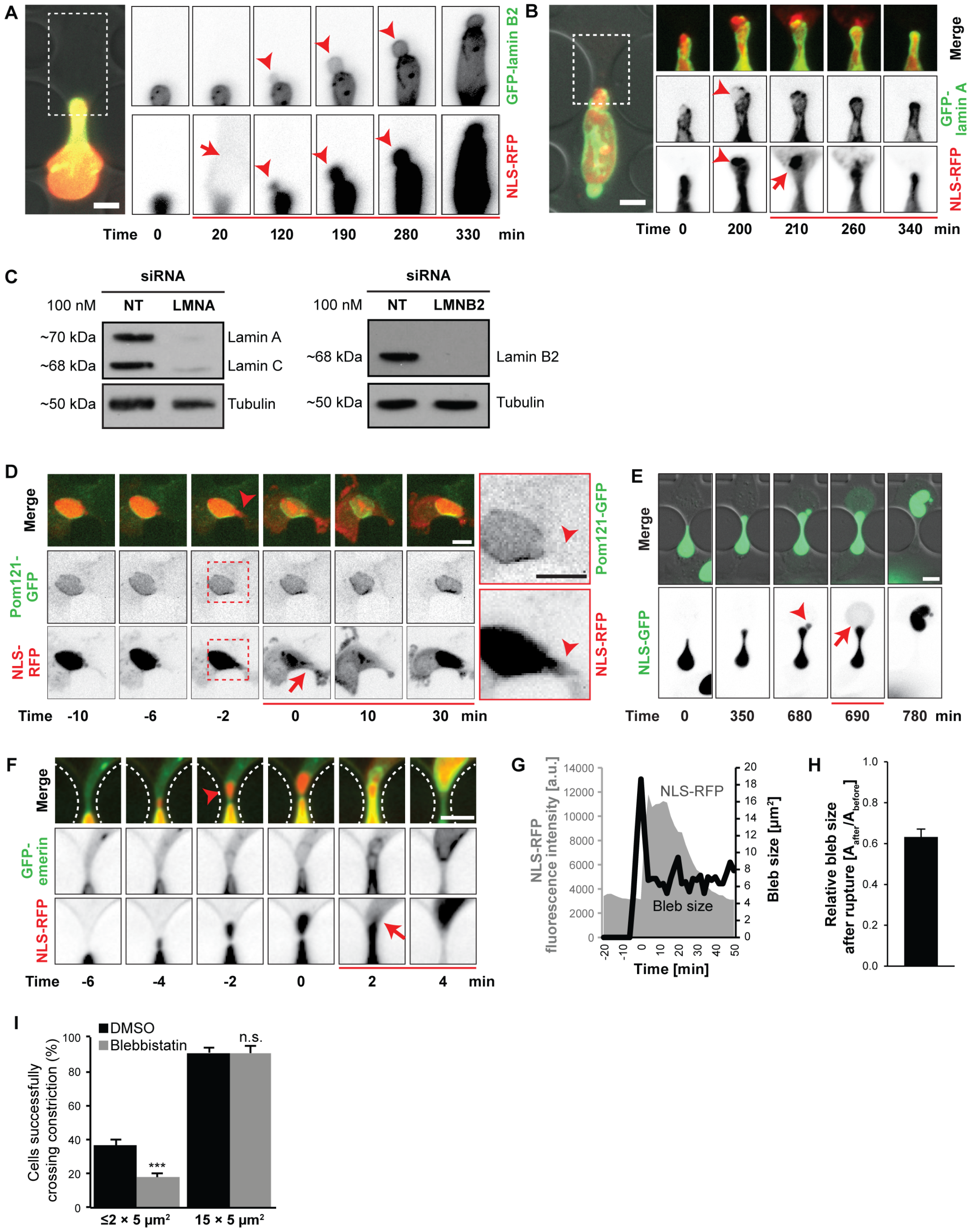

Fig. S10

Molecular details of NE rupture. (**A**) Representative image sequence of an MDA-MB-231 cell (of >150 cells recorded) co-expressing NLS-RFP and GFP-lamin B2 showing that the nuclear bleb initially contains only little lamin B2 compared to the main nucleus (arrowhead), with lamin B2 intensity inside the bleb gradually increasing during bleb expansion. Fluorescence intensities were inverted for better visualization. Here and in the following panels, red arrows and lines below frames indicate beginning and duration of NE rupture(s). Scale bar: 10 µm. (**B**) Representative example of an MDA-MB-231 cell (of >150 cells recorded) co-expressing NLS-RFP and GFP-lamin A showing a bleb with low lamin A intensity (arrowhead), followed by a NE rupture event. Scale bar: 10 µm. (**C**) Western blots confirming the siRNA-mediated depletion of lamins A and C, as well as lamin B2, with tubulin used as loading control. (**D**) Representative example of an HT1080 cell co-expressing NLS-RFP and Pom121-GFP, a trans-membrane nuclear pore complex protein. The forming bleb was devoid of Pom121-GFP (arrowheads). Red dashed line indicates inset location. Scale bars: 10 µm. (**E**) Representative image sequence of an HT1080 cell (of >10 recorded rupture events) depicting nuclear membrane bleb formation (arrowhead) and NE rupture during migration through small constriction. The nuclear bleb collapsed after NE rupture. Scale bar: 10 µm. (**F**) Retraction of nuclear membrane bleb (arrowhead) following NE rupture visualized by co-expression of NLS-RFP and the inner nuclear membrane marker GFP-emerin in an HT1080 cell. Scale bar: 10 µm. (**G**) Corresponding measurement of nuclear bleb size and cytoplasmic NLS-RFP fluorescence intensity to indicate time of NE rupture. (**H**) Relative bleb size after rupture compared to bleb size prior to rupture indicates collapse of bleb after NE rupture. $n = 27$ (**I**) Blebbistatin treatment reduced the percentage of HT1080 cells that were able to migrate through 2×5 µm^2 constrictions, whereas no migratory impairment was found in 15×5 µm^2 constrictions. ***, $p < 0.001$; n= 286, 194, 122 and 54 cells, respectively.

Figure S11

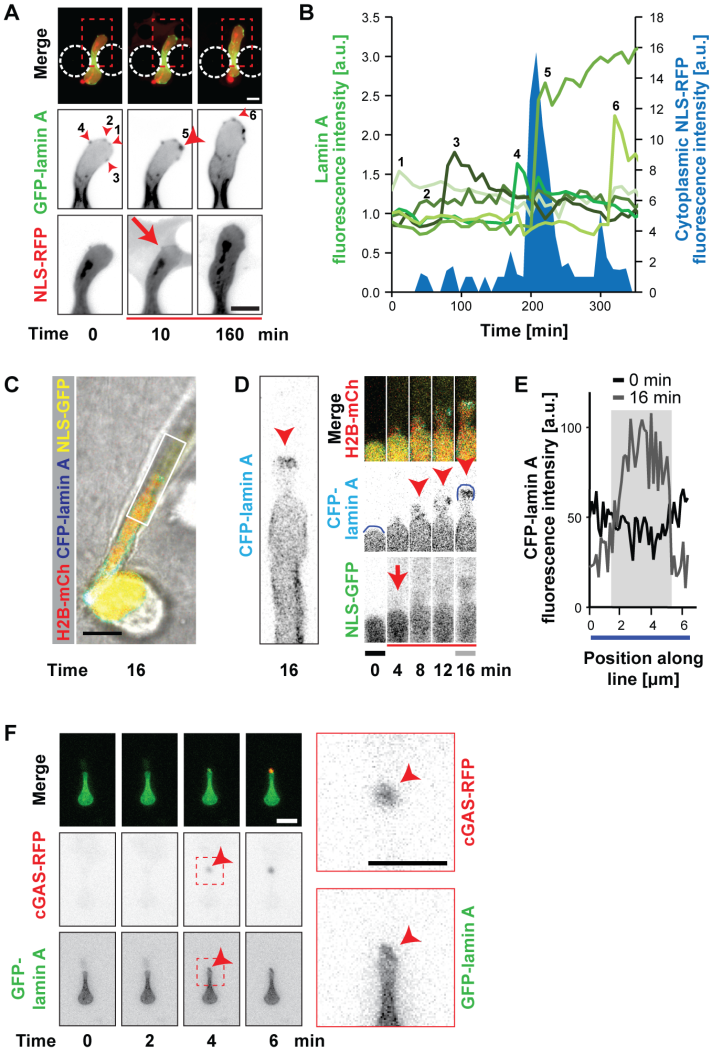

Fig. S11

Accumulation of lamin A at sites of NE rupture. (**A**) Representative example of lamin A accumulation ('lamin scar') in response to NE rupture in an MDA MB 231 cell (of >40 cells recorded). The example contains four scars from previous rupture events (small numbered arrowheads) and shows the formation of a new, larger scar (big numbered arrowhead) after NE rupture. The lamin A accumulations persisted after the cell recovered from the NE rupture. Here and in the following panels, red arrows and lines below frames indicate beginning and duration of NE rupture(s). Scale bar: 10 µm. (**B**) Quantitative analysis of local GFP-lamin A accumulation (green) and NLS-RFP leakage into the cytoplasm (blue) revealing that lamin scars formed upon NE rupture events. Different green lines correspond to different scar formations along the NE, with numbers corresponding to the labeled scars in panel A. (**C-E**) Accumulation of lamin A at sites of NE rupture during HT1080 cell migration in collagen matrices. (C) Overview and (D) close-up of nuclear deformation extending into the cell's leading pseudopod. Arrowheads indicate lamin A accumulation. (E) Corresponding quantification of fluorescence signal intensity along blue lines in (D) indicating lamin A accumulation within 16 minutes. Scale bar: 10 µm. (**F**) Example image sequence of an HT1080 cell moving through migration device that showed GFP-lamin A accumulation (arrowhead) at the site of NE rupture, visualized by cGAS-RFP accumulation (arrowhead). Scale bar: 10 µm, inset: 2 µm.

Figure S12

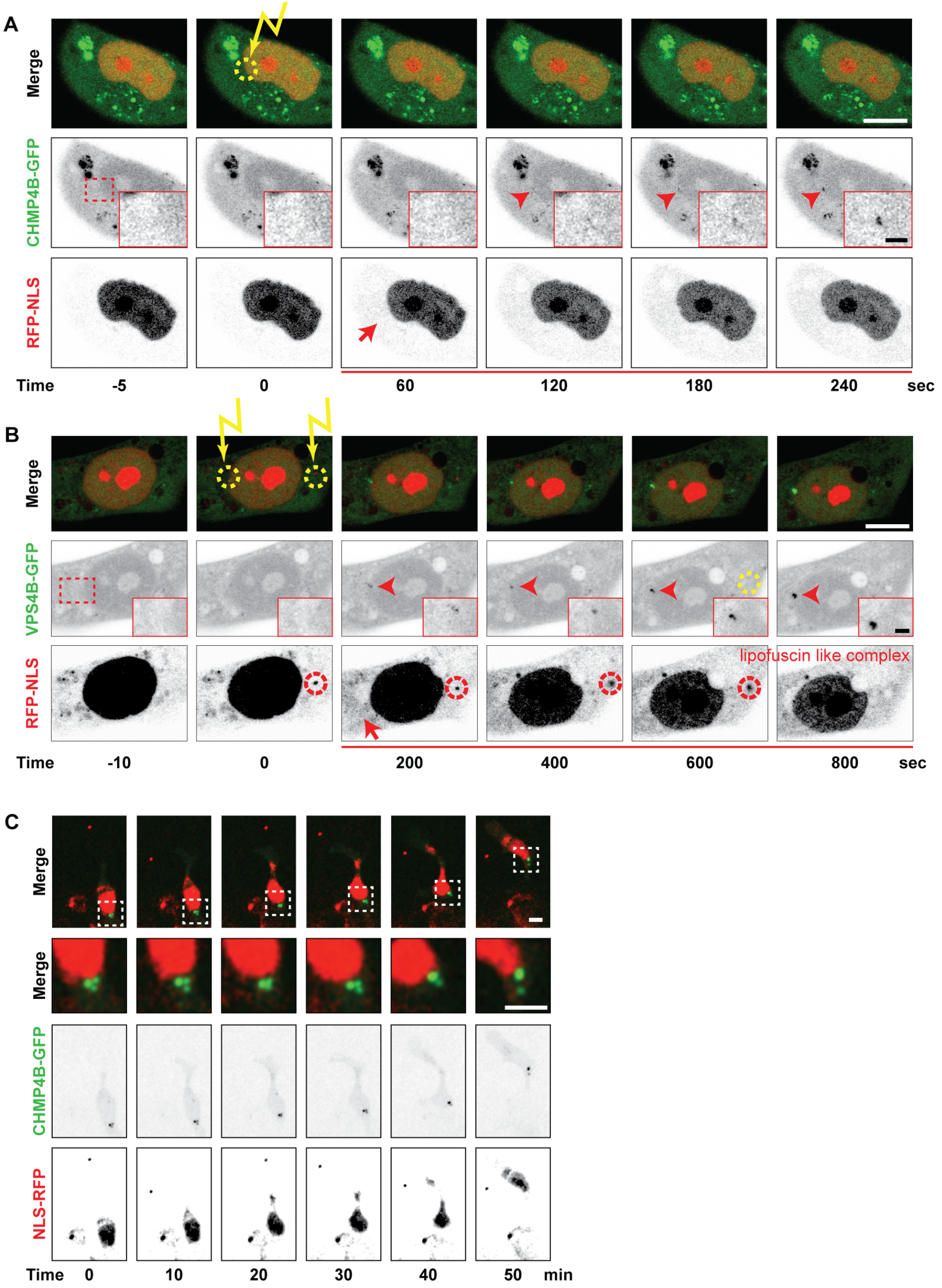

Fig. S12

Accumulation of ESCRT-III machinery at sites of NE rupture. (**A**) Representative image sequence (out of 6 cells recorded) of laser induced disruption of NE integrity in an MDA-MB-231 cell co-expressing CHMP4B-GFP and NLS-RFP, showing rapid accumulation of CHMP4B (arrowhead) at the site of NE rupture (yellow dashed circle). Red dashed box indicates inset location. Here and in all other panels, red arrows and lines below frames indicate beginning and duration of NE rupture(s). Scale bar: 10 µm. (**B**)

Image sequence of laser ablation of the NE in a MDA-MB-231 cell expressing VPS4B-GFP and NLS-RFP, showing accumulation of VPS4B (arrowhead) at the site of the nuclear ablation (left yellow dashed circle). A control region in the cytoplasm (right yellow dashed circle) did not show accumulation of VPS4B, but still showed laser induced lipofuscin-like complexes in the RFP-channel (red dashed circle), indicating that the ablation was successful, but that the targeted recruitment is specific to NE disruption. Red dashed box indicates inset location. Representative example of 6 cells recorded. Scale bar: 2 µm. (**C**) Image sequence of an HT1080 cell expressing CHMP4B-GFP and NLS-RFP migrating through a constriction without NE rupture, demonstrating that CHMP4B does not accumulate at the NE in the absence of NE rupture. Inset: the small cytoplasmic CHMP4B-GFP accumulation near the nucleus is related to other functions of the ESCRT-III family and is not localized at the NE. Dashed boxes indicate inset. Scale bars: 10 µm.

Figure S13

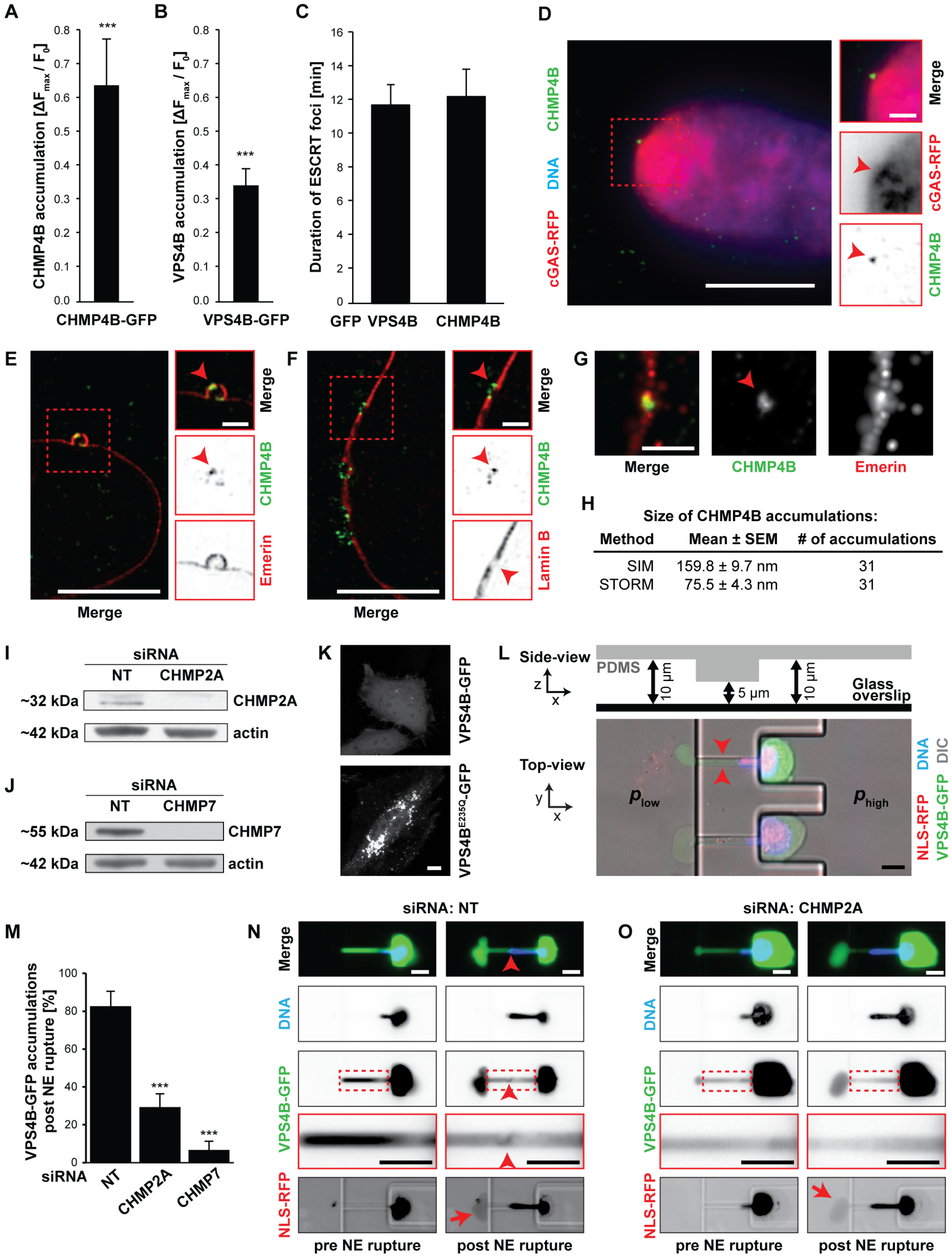

Size of CHMP4B accumulations:

Method	Mean ± SEM	# of accumulations
SIM	159.8 ± 9.7 nm	31
STORM	75.5 ± 4.3 nm	31

Fig. S13

Analysis of ESCRT-III and VPS4B recruitment after NE rupture. (**A**) Quantification of CHMP4B-GFP accumulation at the site of nuclear membrane damage following NE rupture, based on increase in GFP-fluorescence intensity, in MDA-MB-231 cells migrating through microfluidic constriction device. ***, $p < 0.0001$ compared to baseline; $n = 12$ cells. (**B**) Quantification of VPS4B-GFP accumulation at the site of nuclear membrane damage following migration-induced NE rupture, based on increase in GFP-fluorescence intensity. ***, $p < 0.0001$ compared to baseline; $n = 12$ cells. (**C**) Quantification of the duration of CHMP4B (in HT1080 cells) and VPS4B (in MDA-MB-231 cells) accumulation at the NE after migration-induced NE rupture inside the migration device. The difference was not statistically significant ($n = 18$ and 12 cells, respectively). (**D**) Example of HT1080 cell expressing cGAS-RFP after NE rupture induced by cell compression imaged by structured illumination (SIM) microscopy. The site of NE rupture was identified by cGAS-RFP accumulation (arrowhead). Immunofluorescence labeling revealed accumulation of endogenous CHMP4B at the site of NE rupture. Red dashed box indicates inset. Scale bars: 5 µm, 1 µm inset. (**E**) Representative super-resolution SIM image (from 12 cells total) stained for CHMP4B (green) and the inner nuclear membrane protein emerin (red). Red dashed box indicates location of inset. Arrowhead: CHMP4B accumulation at NE rupture site. Scale bars: 5 µm, 1 µm inset. (**F**) Representative super-resolution SIM image of cell (from 12 cells total) labeled for CHMP4B (green) and lamin B (red), showing lack of lamin B at NE rupture site. Red dashed box indicates location of inset. Scale bars: 5 µm, 1 µm inset. (**G**) 3D-dSTORM image of CHMP4B recruitment (arrowhead) following compression-induced NE rupture. Labeling against emerin was used to mark the nuclear membrane; gamma settings have been adjusted for emerin to better visualize the NE. Scale bar: 1 µm. (**H**) Measurements of the CHMP4B accumulation size by two different super-resolution imaging methods. Since the maximal theoretical resolution of SIM is around 115 nm for Alexa Fluor 568, this technique cannot provide accurate size information for features smaller than this size. By carrying out the same measurements on diffraction limited beads, we measured an average size of 159.8 ± 9.7 nm, which we then defined as the experimental limit of size detection using SIM. $n =$ 31 cells for each imaging modality. (**I**) Immunoblot blot analysis to confirm siRNA-mediated depletion of CHMP2A, with actin as loading control. (**J**) Immunoblot analysis to validate siRNA-mediated depletion of CHMP7, with actin as loading control. (**K**) Maximum intensity projection of cells expressing VPS4B-GFP and the ATP hydrolysis mutant VPS4B^{E235Q}-GFP, displaying uniform expression for the wild-type protein and strong accumulations of the mutant form, which prevents ESCRT recycling. Scale bar: 10 µm. (**L**) Overview of 'micropipette' aspiration device to induce NE rupture. The schematic side-view through a micropipette channel (arrowheads) shows the different heights within the device. The corresponding micrograph shows two MDA-MB-231 cells co-expressing VPS4B-GFP and NLS-RFP and Hoechst 33342-labeled DNA (blue) inside the micropipette device. Cells were perfused into the taller pockets and then drawn into the micropipette channels (cross section: 3×5 µm^2) by applying a pressure gradient across the device (p_{high} and p_{low}). Scale bar: 10 µm. (**M**) VPS4B-GFP recruitment to the NE envelope after rupture induced by a micropipette aspiration device. Depletion of CHMP2A and CHMP7 by siRNA decreased the VPS4B recruitment significantly after NE rupture compared to non-target (NT) control. ***, $p < 0.001$; $n = 23$, 41, 30 cells, respectively. (**N**) Examples for VPS4B-GFP recruitment (of $n = 23$ cells) after NE rupture in the micropipette device. Red dashed box indicates location of inset. Arrowhead indicates site of VPS4B recruitment. Arrows indicate NE rupture detected by cytoplasmic NLS-RFP signal. Scale bar: 10 µm. (**O**) Example of a CHMP2A siRNA treated cell (of $n = 41$ cells) lacking the VPS4B-GFP recruitment to the NE in response to micropipette-induced NE rupture. Red dashed box indicates inset. Arrows indicate NE rupture. Scale bar: 10 µm.

Figure S14

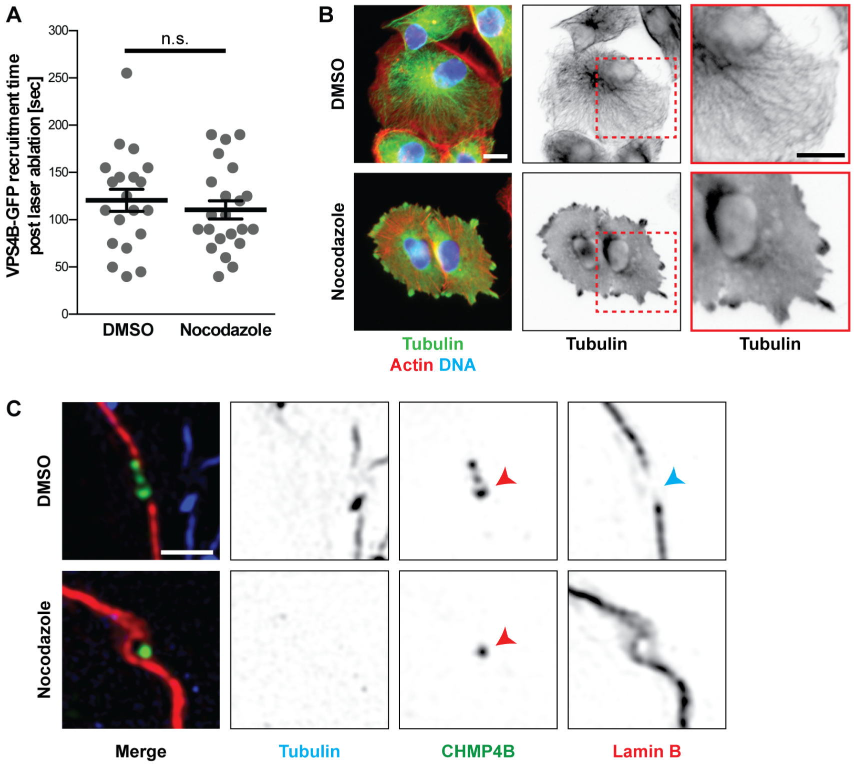

Fig. S14

ESCRT-III and VPS4B recruitment to sites of NE is independent of microtubules. (**A**) Duration of VPS4B-GFP recruitment to the NE rupture site after laser ablation in MDA-MB-231 cells. Nocodazole treatment did not affect the recruitment efficiency of VPS4B-GFP to the NE. *n* = 20, 22 cells, respectively. (**B**) Efficacy of nocodazole treatment was confirmed by imaging microtubule disruption. Representative immunofluorescence images (from ≥20 cells recorded) of tubulin (green), actin (red) and DNA (blue) after treatment with nocodazole or vehicle control (DMSO). Red dashed box indicates location of inset. Scale bar: 10 µm. (**C**) SIM images of vehicle and nocodazole treated cells that had been compressed to induce NE rupture. CHMP4B accumulated (red arrowhead) in both treatments at the NE after rupture. Super-resolution images also confirmed defects/weakness in endogenous lamin B network at sites of NE rupture (blue arrowhead). Representative example from 22 cells recorded. Scale bar: 1 µm.

Figure S15

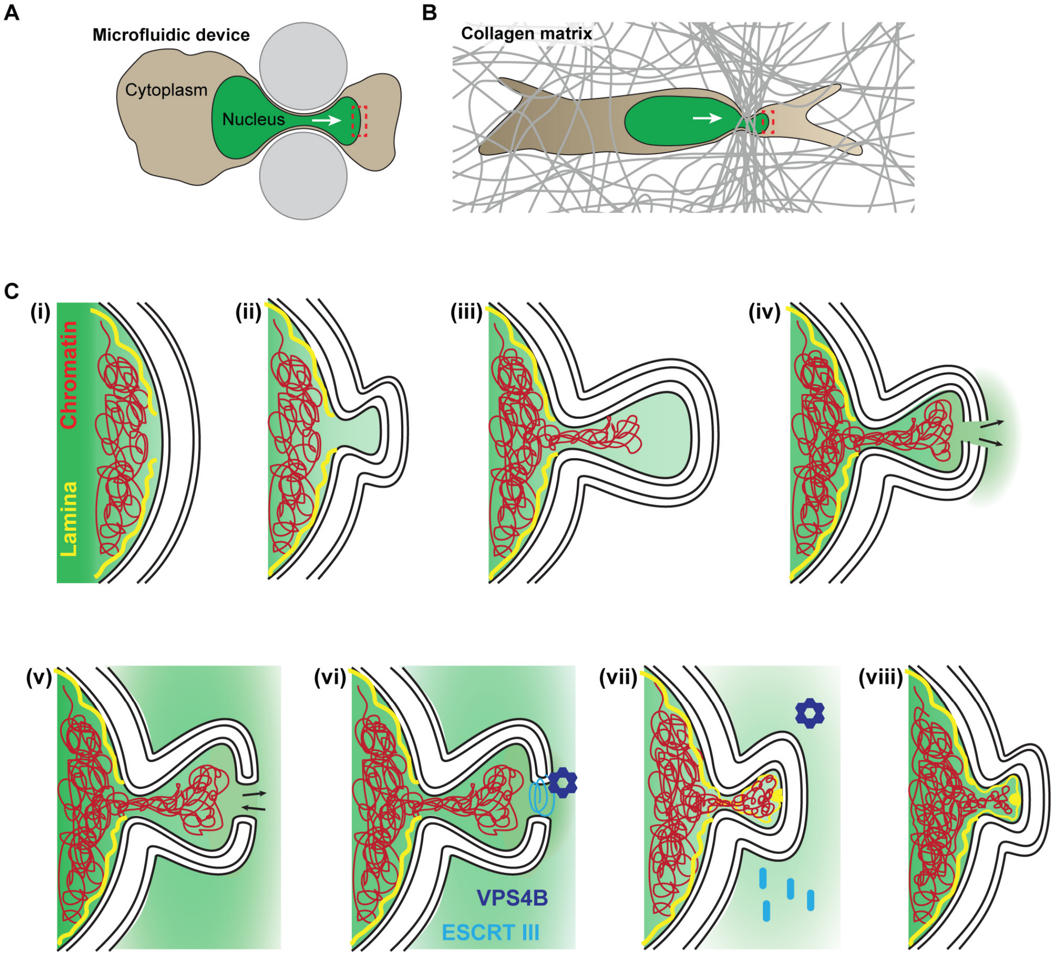

Fig. S15
Proposed biophysical model of nuclear membrane rupture and repair. (**A**) Schematic overview of cell migrating in confining environments in microfluidic device and (**B**) collagen matrix. (**C**) Proposed sequence of events of nuclear bleb formation, membrane rupture, and repair. Increasing nuclear pressure, caused by cytoskeletal forces during migration through tight constrictions, results in increasing stress on the nuclear envelope, particularly in regions with high membrane curvature, such as the tip of the nucleus passing through a constriction. At sites where the nuclear membrane is insufficiently supported by the nuclear lamina, and/or local forces orthogonal to the nuclear membranes are particularly high due to severe membrane curvature, the nuclear membranes can detach from the underlying lamina and form nuclear membrane blebs when the pressure across the nuclear envelope reaches a critical threshold *(ii)*. Pressure-induced expansion of the nuclear membranes (now separated from the supporting lamina), and possibly in combination with membrane recruitment from the endoplasmic reticulum (ER), leads to the formation of a growing nuclear membrane bleb, devoid of nuclear pores and nuclear lamins. Chromatin can protrude across the nuclear lamina into the growing membrane bleb *(iii)*. Ultimately, membrane expansion inside the bleb exceeds the critical areal strain of lipid bilayers, which is less than 5% (*41*), causing NE rupture *(iv)*. Mobile nuclear contents

diffuse into the cytoplasm, and normally cytoplasmic molecules and organelles can enter the nucleus (*12, 13*). Since open membrane ends would be thermodynamically extremely unfavorable, we hypothesize that the damaged and likely retracting inner and outer nuclear membranes rapidly fuse with each other. This results in an annular membrane channel that allows prolonged exchange between the nucleoplasm and cytoplasm *(v)*, resembling the reforming NE in late anaphase (*28, 29*). ESCRT-III subunits (blue spiral) are rapidly recruited to the site of these membrane channels *(vi)*, possibly in response to calcium efflux from the luminal space and ER during the rupture (*39, 42*). ESCRT-III complex components then seal the remaining membrane channels by mediating membrane scission *(vii)*, thereby restoring nuclear membrane integrity *(viii)*, similar to their role in mitosis (*28, 29*). In parallel, accumulation of lamins completes nuclear envelope restoration. This biophysical model is consistent with the key experimental observations and manipulations reported here: (1) nuclear membrane bleb formation preceded or coincided with NE rupture; (2) NE rupture caused (partial) collapse of these blebs as nuclear content spilled into the cytoplasm; (3) nuclear blebs formed at spots of local weakness in the nuclear lamina network, and depletion of lamins increased incidence of nuclear envelope rupture; (4) confinement that required increased nuclear membrane curvature resulted in increased NE rupture, particularly when the smallest dimension of the nucleus approached or fell below 3 μm; and (5) reducing actomyosin contractility resulted in fewer nuclear ruptures during confined migration. Each of these factors alone was insufficient to predict site and timing of NE rupture, but acting together they are responsible for the more than 10-fold increase in NE rupture during confined migration compared to unconfined cells.

Supplementary Movies:

Movie S1

Nuclear rupture in microfluidic device. MDA-MB-231 breast cancer cell migrating through 2 × 5 μm^2 constrictions in microfluidic device. The cell exhibits repetitive nuclear ruptures during passage through the constriction, visualized by transient escape of NLS-GFP from the nucleus into the cytoplasm. Time interval: 10 min.

Movie S2

Nuclear bleb formation and rupture during cell migration in collagen matrix. HT1080 fibrosarcoma cell stably transfected with H2B-RFP (red) and NLS-GFP (green) migrating in fibrillary matrix of rat tail collagen (2.5 mg/mL) in the presence of MMP inhibitor GM6001. Images acquired by confocal microscopy at 37°C. Representative still images of this sequence are shown in Figures 1C, 3C, and S9A-B. Insets show nuclear bleb formation and retraction at the front of the nucleus. Time interval: 4 min. Scale bar, 10 µm; 2 µm (inset).

Movie S3

Nuclear bleb formation and rupture in vivo. HT1080 fibrosarcoma cells co-expressing H2B-RFP (red) and NLS-GFP (green) were transplanted into the mouse dermis in the dorsal skin-fold chamber and tissue-invading cells were monitored by time-lapse multiphoton microscopy. Blood vessels and collagen fibers were visualized by 70 kDa-dextran-Al750 (magenta) and SHG (cyan), respectively. To increase visibility of the weak cytoplasmic GFP signal, the nuclear rupture event is displayed in gray scale. Red arrowheads mark nuclear bleb formation preceding cytoplasmic leakage of NLS-GFP (red ellipse). The cell at the bottom right also exhibits a nuclear rupture at the beginning of the sequence. Time interval: 3min.

Movie S4

Chromatin herniation in migrating cell in collagen in vitro. HT1080 fibrosarcoma cells stably co-expressing H2B-RFP (red) and GFP-lamin A (green) migrated in rat tail collagen (3.3 mg/mL) in the presence of MMP inhibitor GM6001. Cells were imaged by confocal microscopy at 37°C. Red arrowheads mark chromatin protrusions across the nuclear lamina; white/black arrowheads mark signal loss of lamin A; and green arrowheads mark lamin A scar formation. Rectangle shows zoom-in area. Representative still images are shown in Figure S7D. Time interval: 2.5 min. Scale bars: 10 µm.

Movie S5

Chromatin herniation in migrating cell in vivo. HT1080 fibrosarcoma cells co-expressing H2B-RFP (red) and GFP-lamin (green) were injected in the mouse dermis in the dorsal skin-fold chamber and monitored by time-lapse multiphoton microscopy. Collagen fibers were visualized with second-harmonic generation (SHG, blue). Inset: Arrowhead marks chromatin herniation during migration. Time interval: 3 min.

Movie S6

Nuclear rupture and fragmentation in breast cancer cells migrating through narrow constrictions. MDA-MB-231 breast cancer cells expressing NLS-GFP and H2B-mCherry. Two cells (starting in the bottom center) display repeated nuclear ruptures and eventually nuclear fragmentation after passage through the 2×5 µm^2 constriction. Note that some cells only express NLS-GFP, without H2B-mCherry. Time interval: 10 min.

Movie S7

CHMP4B-GFP transiently localizes to the site of NE rupture. HT1080 cell co-expressing CHMP4B-GFP and NLS-RFP migrating through a 2×5 µm^2 constriction. Video shows formation of a nuclear bleb (black arrow) prior to nuclear rupture (red arrow) and subsequent rapid and transient recruitment of CHMP4B-GFP to the site of nuclear rupture (white arrowhead). Time interval: 2 min.